MODELING OF SHEAR STRENGTHENING OF REINFORCED CONCRETE BEAMS RETROFITTED WITH EXTERNALLY BONDED FIBER REINFORCED POLYMERS

A Thesis

Submitted to the Graduate Faculty of the
Louisiana State University and
Agricultural and Mechanical College
in partial fulfillment of the
requirements for the degree of
Master of Science in Civil Engineering

in

The Department of Civil and Environmental Engineering

by
Srinivasa Anusha Bellamkonda
B. Tech, JNTU, India, 2009
May 2013

ACKNOWLEDGEMENTS

I would like to extend my first and foremost appreciation towards my advisor, Dr. Michele Barbato for his constant guidance and immense support throughout my research, without which this work would have not been possible. I would also like to thank my graduate committee members, Dr. Ayman Okeil and Dr. Steve Cai, for their support and technical guidance in developing the contents of this thesis. I thank Ms. Julie Mueller and Ms. Janet Labatut of Civil Engineering for assisting me with various departmental issues.

I would like to express my immense love and gratitude towards my parents, Eswar Kumar and Padmavathi, for all their love, support and prayers. Their constant encouragement in my studies has made me achieve my goals. I will always love my little brother, Anirudh, for always protecting me like an elder brother and for giving me many moments of laughs and silly fights, which I will cherish throughout my life.

My sincere appreciation goes to Dr. Janna Oetting for employing me as a graduate assistant. Her concern towards me and my family well-being has always created a warm atmosphere throughout my course at LSU.

I would also like to thank the Louisiana Board of Regents (LA BoR) through the Louisiana Board of Regents Research and Development Program, Research Competitiveness (RCS) subprogram, under Award No. LESQSF (2010-13)-RD-A-01

I would also like to thank my research colleagues, Vipin and Clara, for their invaluable help towards my research. I thank my friends Rasagnya, Trina, Asmita, Srujana, Chaitanya, Jai, Sarat, Surendra, Murthy, Sundeep, Shiva, Shiny and many others, for their love and support.

TABLE OF CONTENTS

LIST OF TABLES

LIST OF FIGURES

ABSTRACT

This thesis presents a study on the shear retrofit of reinforced concrete (RC) beams with externally bonded fiber reinforced polymers (FRP), since it is very important for RC beam to have a shear strength that is higher than the flexural strength in order to ensure ductile flexural failure mode. The study proposes a new model to predict the FRP shear strength contribution for different modes of failure, i.e., bending, shear with FRP rupture, shear with FRP debonding, and mixed shear-flexure and various retrofit techniques, i.e., side-bonding, U-jacketing, and full wrapping. The proposed model is compared to other existing models for FRP shear strength contribution, which are available in the literature. This comparison is made in terms of model prediction capabilities for experimentally measured shear strength increments due to FRP retrofit, which are also taken from previous literature studies. It is observed that the proposed model is in overall in good agreement with the experimental data.

Furthermore, the results of this study are used to formulate a general-purpose frame finite element (FE) to compute the load carrying capacity and predict the behavior of RC beams when retrofitted with externally bonded FRP in shear. The finite element is extended to model a two dimensional frame structure with strong columns and weak beams that are deficient in shear. It is found that the proposed frame FE captures well the increase in load carrying capacity of the frame structures.

1. INTRODUCTION

Flexural failure and shear failure are the two primary modes of failure in reinforced concrete (RC) beams. Flexural failure of a beam is ductile in nature, i.e., it occurs gradually with large deflections and cracking, which provide a warning of incipient failure. Conversely, shear failure is brittle in nature and does not allow substantial redistribution of loads; thus, shear failure occurs without any prior warning and is often catastrophic. Poorly designed beams may fail in shear before reaching the flexural strengths. Hence, RC beams must have sufficient shear strength, higher than flexural strength, in order to ensure a ductile failure mode.

Shear failure of RC structures may be due to many factors, e.g., insufficient shear reinforcement, reduction of steel area due to corrosion and spalling of concrete caused by aggressive environmental conditions, increased service load due to change in usage of the structure, and any detailing, design, and/or construction error. Thus, strengthening and rehabilitation of RC structures may be needed to increase the ultimate load carrying capacity of shear-deficient beams. Structures that are deficient in shear can be strengthened or repaired by using various methods, e.g., external prestressing, shortcreting, polymer impregnation, steel plate bonding [1]. Among these retrofit solutions, the use of externally bonded fiber reinforced polymers (FRPs) is becoming more frequently used and widely recognized by modern design codes and guidelines [2][3].

FRP shear retrofit of RC structures presents numerous advantages compared to other more traditional techniques, e.g., light weight and ease of installation, high strength to weight ratio, high stiffness to weight ratio, and corrosion resistance. However, the accurate prediction of the shear strength of FRP-retrofitted beams is a complex task.

1.1 Research motivations

Shear retrofit of RC beams with externally bonded FRP is being widely recognized as an efficient retrofit technique. In recent years, many experimental studies have been carried out and several models have been implemented in modern design codes and guidelines [2][3]. However, modeling of RC structures retrofitted in shear using FRP is a complicated task and represents an active research field, owing to the difficulty in interpreting the various factors simultaneously contributing to multiple resisting mechanisms. The interaction between these resistance mechanisms are very complex and still need to be predicted more accurately. Hence, reliable and robust finite element (FE) models and formulations are needed to allow engineers to model FRP strengthened RC structures and to predict their structural response and performance under different strengthening configurations.

1.2 Objectives

The objectives of this research are: (a) comparing the accuracy of existing models for computing the increment of shear strength obtained using FRP retrofit; (b) developing a new improved model for shear strength increment due to FRP retrofit; (c) implementing this new model into a force-based FE beam model to be used within a general-purpose nonlinear FE program; (d) extend the FE beam model to analyze a two dimensional frame element. This FE model needs to be able to predict the failure mechanism and estimate the load carrying capacity of RC beams with various FRP shear retrofit techniques.

1.3 Thesis outline

This thesis consists of six chapters: Chapter 1 is an introduction to the problem of RC beams retrofitted in shear using externally bonded FRPs.

Chapter 2 presents a literature review of shear failure mechanisms of RC beams retrofitted in shear with externally bonded FRP and existing models for computing the shear strength of RC beams with FRP shear retrofit.

Chapter 3 introduces a newly proposed model for computing the FRP shear strength contribution and presents the comparison between FRP shear contributions that are experimentally measured and numerically computed using different FRP shear models for RC beams failing in pure shear.

Chapter 4 describes the frame FE developed in this study. The modeling capabilities of this FE are studied in terms of prediction of failure mechanism and load carrying capacity of RC beams retrofitted in shear using FRPs.

Chapter 5 presents the FE analysis of a two-dimensional RC frame structure with FRP shear retrofit which is modeled using the frame FE developed in this study.

Finally, Chapter 6 presents the conclusions of this study and recommendations for future research.

2. LITERATURE REVIEW

2.1 Shear failure mechanisms in RC beams

Shear failure of RC beams is mainly caused by the formation of diagonal tension cracks within the web of the beam, which can become unstable and fail [4]. In order to resist the shear stresses produced by the applied loads, the beam web develops several shear transfer mechanisms: (a) shear resistance developed by the uncracked concrete in the compression zone (V_{cc}); (b) interface shear transfer by aggregate interlocking in the cracked concrete (V_{ca}); (c) dowel action of the longitudinal reinforcement (V_d); and (d) residual tensile stresses across the cracks (V_{cr}). The shear resistance provided by the uncracked concrete depends on the depth of the intact concrete. The interfacial shear transfer by the aggregates decreases with decrease in the aggregate size and increase in crack width. The resistance provided by the dowel action is dependent on the ratio of the longitudinal reinforcement (ρ) and the concrete cover (c).

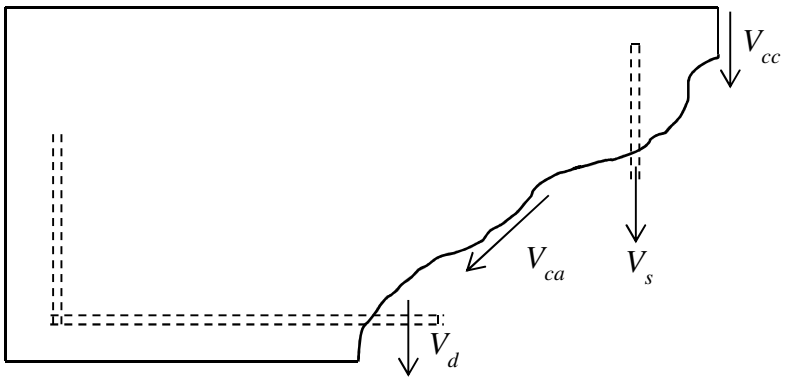

Figure 2-1: Shear force transfer mechanism (adapted from [4])

Thus the shear failure mechanism of a RC beams depends mainly on the compressive strength of the concrete (f_c), effective depth of the beam (d), maximum aggregate size (d_a), and shear span to depth ratio (a/d). The behavior of beams failing in shear can be studied with respect to the different shear span to depth ratio. Three different cases can be considered:

(a) Short shear span beams, which have *a/d* smaller or equal than 2.5. Beams having very short shear spans, i.e., *a/d* less than one, are generally referred to as deep beams. Such beams develop inclined cracks joining the load and support. Thus, the beam develops an arch action, thereby destroying the horizontal shear flow from the longitudinal steel to the compression zone. The reinforcement behaves as a tension tie in a tied arch. Such beams fail by anchorage failure at the ends of the tension tie.

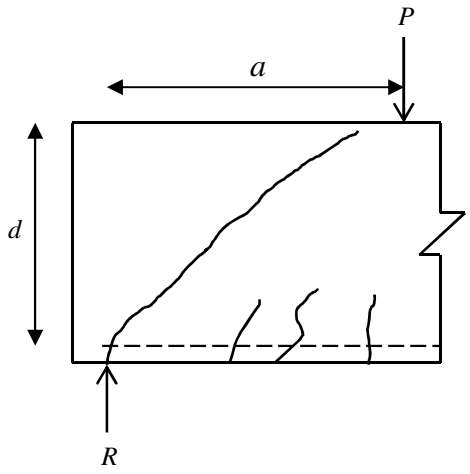

Figure 2-2: Concrete compression diagonal crushing

Short shear span beams with *a/d* between 1 and 2.5 initially develop small flexural cracks on the tension face of the beam. However, these cracks are intersected by the longitudinal reinforcement and do not progress further. The beams also develop an inclined crack referred to as web shear crack, which propagates towards the neutral axis. Simultaneously, crushing of concrete occurs in the top compression fibers along with redistribution of loads. This causes a reduction in the progression rate of the shear crack. However, sudden failure occurs when the principal inclined shear crack reaches the crushed concrete zone as shown in Figure 2-3. This type of failure is referred to as shear compression failure.

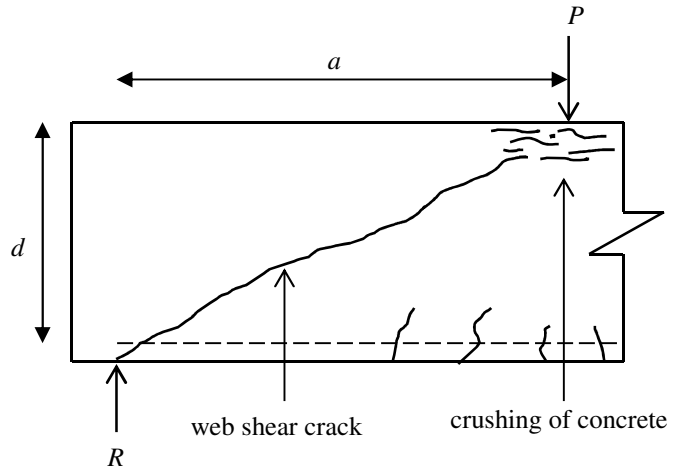

Figure 2-3: Shear compression failure in beams with $1 < a/d < 2.5$

(b) Slender beams, which have shear spans with *a/d* contained between 2.5 and 6. These beams initially develop flexural cracks, which are more or less vertical into the beam. These cracks cause stress concentration near the head of the cracks owing to the altered state of stress in the beam. For increasing load, the flexural cracks extend to become shear cracks. This diagonal shear crack encounters resistance as it propagates up into the compression zone. With further increase in load the crack extends gradually at a flatter slope until sudden failure occurs. This type of failure is known as diagonal tension failure.

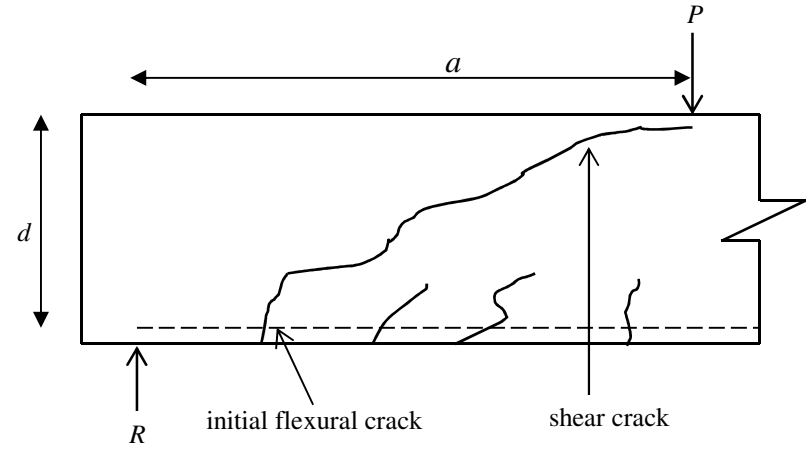

Figure 2-4: Diagonal tension failure in beams with $2.5 \leq a/d \leq 6$

(c) Beams with very slender shear spans (i.e., *a/d* greater than 6), which fail in flexure before the formation of the diagonal tension cracks. The failure is initiated by the yielding of the tension reinforcement, eventually resulting in concrete crushing at the section with maximum bending moment or rupture of the longitudinal steel reinforcement in tension.

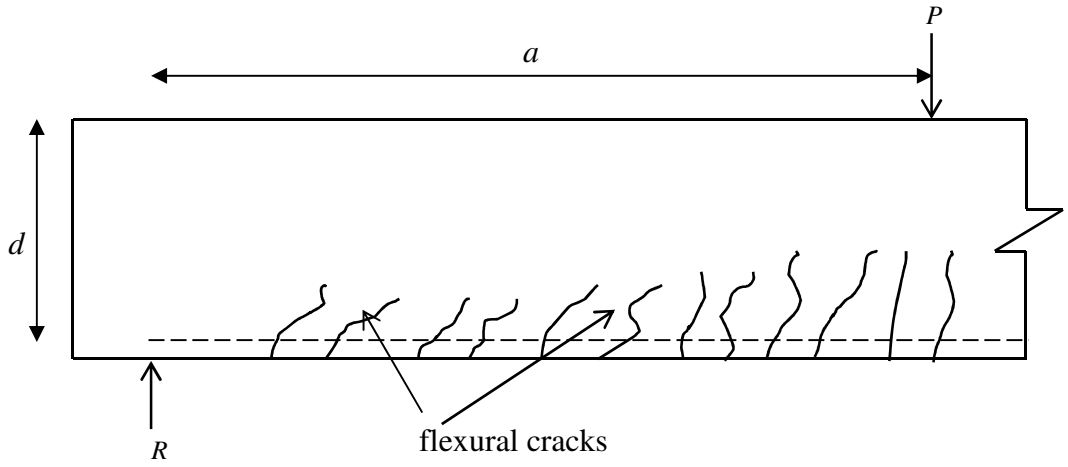

Figure 2-5: Flexural failure in beams with *a/d* > 6

2.2 FRP retrofitting

Externally bonded FRP sheets and plates cans be used for strengthening of RC members in flexure, shear and confinement. In particular, the following different configurations of externally bonded FRP are used to improve the shear capacity of RC beams: (a) bonding FRP to the side of the beam, i.e., side bonding (S); (b) bonding FRP on both sides and the tension face of the beam, i.e., U-jacketing (U); and (c) wrapping FRP around the whole cross section of the beam, i.e., full wrapping (W). In general, FRP can be applied to the RC beam as continuous sheets or discontinuous strips. FRP sheets and plates have maximum strength in the direction of the fibers; thus, they can be oriented with different angles with respect to the beam axis in order to prevent the formation and propagation of shear cracks. However, shear forces in a beam can change

direction in case of reversed cyclic loads, e.g., earthquake loads. Thus, FRPs can be placed in two different directions to account for such cases. Different combinations of fiber distribution and fiber orientation produce different strengthening schemes. FRP can also be applied in multiple layers of sheets or strips to increase the overall thickness of the FRP. The different configurations of FRP shear reinforcement are shown in Figure 2-6.

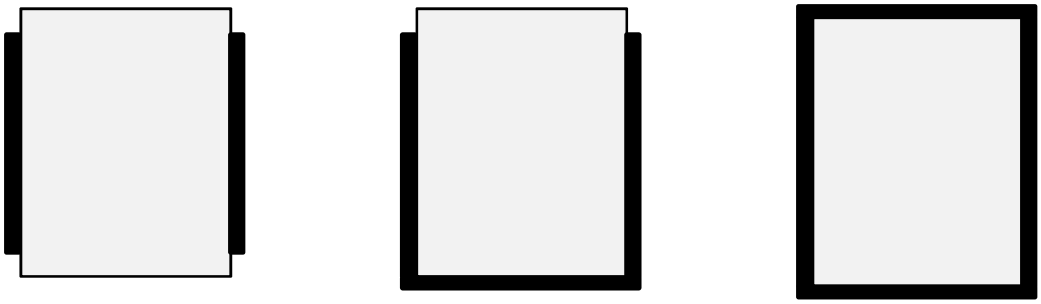

Figure 2-6: FRP shear strengthening techniques (cross-section view)

2.3 Failure modes for RC beams with FRP shear retrofit

RC beams strengthened with externally bonded FRP primarily experience the following potential failure modes:

a) Concrete compression diagonal crushing

The forces in the FRP sheets/strips are directly proportional to the diagonal compressive stresses developed in the concrete struts. When these stresses exceed the concrete compressive strength, crushing of concrete occurs. This failure is highly dependent on the crack angle and the FRP fiber orientation. The flatter is the crack angle, the larger are the stresses developed.

b) Tensile rupture of FRP

Tensile rupture of FRP generally occurs due to the diagonal tension at the shear cracks. Initial cracking starts with vertical flexural cracks, which originate from the tensile face of the

beam and propagate towards the loading point, then forming an inclined crack due to the diagonal tension. With the increase in width of the shear crack, the maximum strain in the FRP eventually reaches the FRP ultimate strain often occurring at the crack end. As the FRP reaches its ultimate strength, it is immediately torn at the maximum stress location. This initial rupture then propagates along the shear crack in the beam, ultimately leading to its failure. It is observed that the effective tensile strength of FRP can be much smaller than the ultimate tensile strength. Such failures are very brittle owing to the brittle nature of FRP.

c) Debonding of FRP from sides of RC beams

Shear failure can be produced by FRP debonding from the sides of the RC beam. This phenomenon is due to the fact that excessive straining of FRP results in strain incompatibilities within the substrate material, leading to cracking. The cracking causes stress concentrations thus producing local debonding. Poor use of adhesive and concrete surface preparation can also result in FRP debonding, thus highly reducing the load carrying capacity of the retrofitted RC beam.

2.4 Computation of shear strength of RC beams retrofitted with FRP in shear

The total shear strength, at a given section V_t, of a RC beam can be expressed as

$$V_t = \min\left(V_{R,max}, V_c + V_s + V_{frp}\right) \tag{2.1}$$

where V_c is the shear strength contribution of concrete, V_s is the shear strength contribution of transversal steel, V_{frp} is the shear strength contribution of FRP, and $V_{R,max}$ is the strength of concrete strut given by

$$V_{R,max} = 0.9 \cdot d \cdot \nu \cdot f_c \left(\frac{1}{\tan\phi + \cot\phi}\right) \tag{2.2}$$

$$\nu = \max\left(0.5, 0.7 - \frac{f_c}{250}\right) \qquad (\text{units: MPa}) \tag{2.3}$$

where ϕ is the angle between the compression strut and the beam axis, f_c is the concrete compressive strength, and d is the beam effective depth.

2.4.1 General nomenclature and notation

This section defines the notation adopted in this study for the geometric and mechanical properties of the beams and the materials affecting the shear strength of FRP retrofitted RC beams (see Figure 2-7).

2.4.1.1 Geometric properties

d = effective depth of the beam

b_w = width of the web

H = total height of the beam

a = shear span of the beam

a/d = shear span to depth ratio

A_{sb} = area of longitudinal steel in the tension side of the beam

A_{st} = area of longitudinal steel in the compression side of the beam

A_{sv} = area of transverse steel

ρ_{sl} = longitudinal steel to cross section area ratio

ρ_{sv} = transverse steel to cross section area ratio

θ = crack angle

w_{frp} = width of the FRP reinforcement

s_{frp} = center to center spacing of the FRP reinforcement

t_{frp} = thickness of the FRP sheet/strip

d_f = effective depth of FRP

α = angle of FRP fiber orientation

A_{frp} = area of the FRP sheet/strip

ρ_{frp} = ratio of FRP reinforcement

L_a = available bond length of the FRP sheet/strip

2.4.1.2 Mechanical properties

f_y = yield strength of longitudinal steel

f_{yv} = yield strength of transverse steel

f_c = compressive strength of concrete

E_{frp} = modulus of elasticity of the FRP

$f_{frp,u}$ = ultimate tensile strength of the FRP sheet/strip

$\varepsilon_{frp,u}$ = ultimate strain in the FRP sheet/strip

$f_{frp,e}$ = effective tensile strength of the FRP sheet/strip

$\varepsilon_{frp,e}$ = effective strain in the FRP sheet/strip

L_e = effective bond length of the FRP sheet/strip

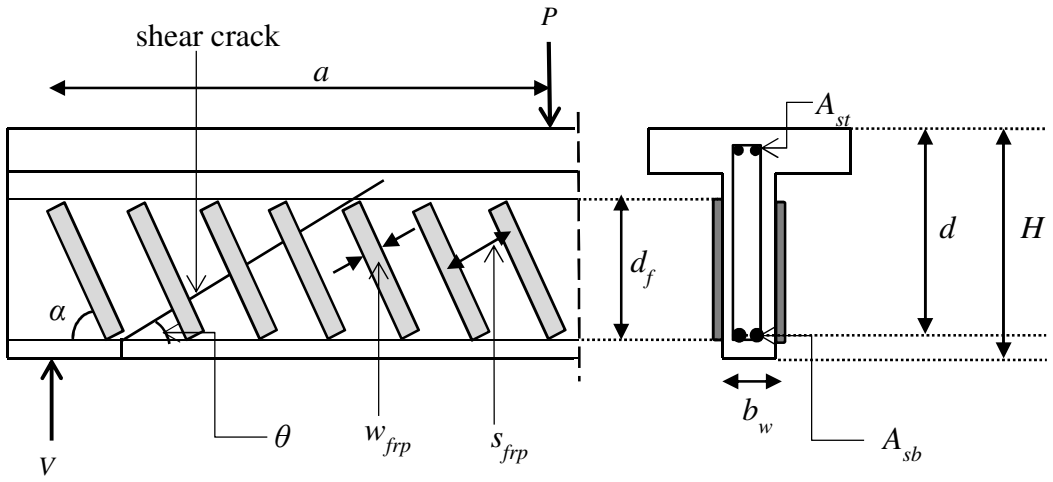

Figure 2-7: General nomenclature and notation (geometric properties)

2.4.2 Shear strength contribution of concrete and transversal steel

The complex nature of estimating the shear strength contribution of concrete in RC beams is attributed to the heterogeneous nature of concrete and the reinforcement, as well as to the complex shear transfer mechanisms after the formation of cracks. To predict this shear strength contribution many researchers [4]-[13] have proposed numerous mechanical models based on fracture mechanics, and empirical models based on simplified mechanical behaviour, often in combination with regression analysis and experimental results. Compressive strength of concrete, effective depth of beam, shear span to depth ratio, longitudinal reinforcement ratio, axial forces are some of the parameters that affect the concrete shear strength contribution.

The shear strength contribution of the transversal steel is computed by assuming that the steel intersected by the shear crack yields at failure. Area of steel, yield strength of the steel, spacing of the stirrups (s), and effective depth of the beam are the factors influencing the shear strength contribution of the transversal steel. This shear strength contribution, V_s, can be computed as,

$$V_s = \frac{0.9 \cdot d \cdot A_s \cdot f_y}{s} \cdot \left(\sin\beta + \cos\beta\right) \tag{2.4}$$

where β is the angle of inclination of the stirrups with respect to the beam axis.

2.4.3 Shear strength contribution of FRP

The shear capacity of FRP sheet/strip depends on various factors, e.g., thickness of the FRP sheet/strip applied on the concrete surface, modulus of elasticity of FRP, compressive strength of concrete, fiber orientation of the FRP, application technique of the FRP. Understanding the shear failure mechanisms and predicting the shear strength contribution of FRP has been the object of study for many researchers [22]-[34]. Some of the existing models are discussed and presented in the following sections.

2.4.3.1 ACI 440 model [3]

The FRP shear strength contribution suggested in ACI 440 [3] is based on the study presented in [15][16] and is given by

$$V_{frp} = \frac{A_{frp} \cdot f_{frp,e} \cdot (\cos\alpha + \sin\alpha) \cdot d_f}{s_{frp}} \tag{2.5}$$

where

$$A_{frp} = 2 \cdot n \cdot t_{frp} \cdot w_{frp} \tag{2.6}$$

$$f_{frp,e} = \varepsilon_{frp,e} \cdot E_{frp} \tag{2.7}$$

in which n is the number layers of FRP sheet/strip applied

$$\varepsilon_{frp,e} = \begin{cases} 0.004 \le 0.75 \cdot \varepsilon_{frp,u} & (\text{for full wrapping}) \\ k_v \cdot \varepsilon_{frp,u} \le 0.004 & (\text{for U-jacketing and side bonding}) \end{cases} \tag{2.8}$$

$$k_v = \frac{k_1 \cdot k_2 \cdot L_e}{11{,}900 \cdot \varepsilon_{frp,u}} \le 0.75 \tag{2.9}$$

$$L_e = \frac{23{,}300}{(n \cdot t_{frp} \cdot E_{frp})^{0.58}} \qquad (\text{units:N, mm}) \tag{2.10}$$

$$k_1 = \left(\frac{f_c}{27}\right)^{\frac{2}{3}} \qquad (\text{units: MPa}) \tag{2.11}$$

$$k_2 = \begin{cases} \dfrac{d_f - L_e}{d_f} & (\text{for U-jacketing}) \\ \dfrac{d_f - 2 \cdot L_e}{d_f} & (\text{for side bonding}) \end{cases} \tag{2.12}$$

2.4.3.2 Triantafillou's model [17][18]

The effectiveness of the load carrying capacity of the externally bonded FRP shear reinforcement at the ultimate limit state depends on the mode of failure of the FRP, i.e., FRP debonding or FRP tensile fracture. The FRP tensile fracture can occur at a stress lower than the FRP tensile strength owing to the stress concentrations at rounded corners or debonded areas. However, it is difficult to know which mode of failure will occur, since the failure mode depends on a combination of various factors such as bond conditions, available anchorage length, type of attachment at the FRP curtailment, thickness of FRP sheet/strips, modulus of elasticity of FRP and concrete. In practice, the actual mechanism is a combination of both peeling and tensile fracture of the FRP. Based on the above considerations, Triantafillou [17][18] proposed a semi-qualitative approach to determine the shear strength contribution of externally bonded FRP, in which the shear strength contribution due to FRP was given by

$$V_{frp} = 0.9 \cdot d \cdot b_w \cdot \rho_{frp} \cdot E_{frp} \cdot \varepsilon_{frp,e} \cdot (1+\cot\alpha) \cdot \sin\alpha \tag{2.13}$$

where

$$\rho_{frp} = \frac{2 \cdot t_{frp}}{b_w} \cdot \frac{w_{frp}}{s_{frp}} \tag{2.14}$$

The value of the effective strain of the FRP, $\varepsilon_{frp,e}$, was determined by a combination of qualitative analysis and calibration of Equation (2.13) with experimental results. The following relations were suggested:

$$\varepsilon_{frp,e} = \begin{cases} 0.17\left(\dfrac{f_c{}^{2/3}}{E_{frp}\cdot\rho_{frp}}\right)^{0.30}\cdot\varepsilon_{frp,u}\,; & \text{for fully wrapped carbon FRP} \\ \min\left[0.65\cdot\left(\dfrac{f_c{}^{2/3}}{E_{frp}\cdot\rho_{frp}}\right)^{0.56}\cdot 10^{-3}, 0.17\cdot\left(\dfrac{f_c{}^{2/3}}{E_{frp}\cdot\rho_{frp}}\right)^{0.30}\cdot\varepsilon_{frp,u}\right]; & \text{for U-jacketing or side bonding of carbon FRP} \\ 0.048\left(\dfrac{f_c{}^{2/3}}{E_{frp}\cdot\rho_{frp}}\right)^{0.47}\cdot\varepsilon_{frp,u}\,; & \text{for fully wrapped aramidic FRP} \end{cases} \quad (\text{units:MPa})$$

(2.15)

2.4.3.3 Cheng-Teng's model [19][20]

According to Cheng and Teng [19][20], the strain distribution in the FRP along a shear crack is non-uniform, since the width of the shear crack varies along its length. With FRP shear retrofit, the failure process starts when the most highly stressed point in the FRP intersected by the shear crack reaches the ultimate tensile strength of FRP. Thus, the FRP does not reach its ultimate tensile strength along the entire crack length and the effective stress carried by the FRP is a fraction of its tensile strength. The FRP shear strength contribution is given by

$$V_{frp} = 2\cdot f_{frp,e}\cdot w_{frp}\cdot t_{frp}\cdot\frac{d_{frp,e}\cdot(\cot\theta+\cot\alpha)}{s_{frp}}\cdot\sin\alpha \tag{2.16}$$

in which

$$d_{frp,e} = z_t - z_b \tag{2.17}$$

$$z_t = \max\left(0.1\cdot d, d_{frp,t}\right) - 0.1\cdot d \tag{2.18}$$

$$z_b = \left[d - \left(h - d_{frp}\right)\right] - 0.1\cdot d \tag{2.19}$$

where $d_{frp,e}$ is the effective height of the FRP bonded on both sides, z_t is the coordinate of the top edge of the FRP, z_b is the coordinate of the lower edge of the FRP, $d_{frp,t}$ is the distance from the beam compression side to the top edge of FRP, d_{frp} is the distance from the beam compression side to the lower edge of FRP.

The effective stress carried by the FRP is given as

$$f_{frp,e} = D_{frp} \cdot \sigma_{frp,max} \tag{2.20}$$

where $\sigma_{frp,max}$ is the maximum stress in the FRP, D_{frp} is the stress distribution factor for FRP.

In case of failure by FRP rupture, the equations for $\sigma_{frp,max}$ and D_{frp} are

$$D_{frp,R} = \frac{1+\zeta}{2} \tag{2.21}$$

$$\zeta = \frac{z_t}{z_b} \tag{2.22}$$

$$\sigma_{frp,max,R} = f_{frp,u} \tag{2.23}$$

In case of failure by FRP debonding, the equations for $\sigma_{frp,max}$ and D_{frp} are

$$D_{frp,D} = \begin{cases} \dfrac{2}{\pi \cdot \lambda} \cdot \dfrac{1-\cos\left(\dfrac{\pi}{2} \cdot \lambda\right)}{\sin\dfrac{\pi}{2} \cdot \lambda} & ;\text{for } \lambda \le 1 \\ 1 - \dfrac{\pi - 2}{\pi \cdot \lambda} & ;\text{for } \lambda > 1 \end{cases} \tag{2.24}$$

$$\sigma_{frp,\max,D} = \min \begin{cases} f_{frp,u} \\ 0.427 \cdot \beta_w \cdot \beta_L \cdot \sqrt{\dfrac{E_{frp} \cdot \sqrt{f_c}}{t_{frp}}} \end{cases} \qquad (\text{units: N, mm}) \tag{2.25}$$

where

$$\beta_L = \begin{cases} 1 & if\ \lambda \geq 1 \\ \sin\left(\dfrac{\pi \cdot \lambda}{2}\right) & if\ \lambda < 1 \end{cases} \tag{2.26}$$

$$\lambda = \frac{L_{max}}{L_e} \tag{2.27}$$

$$L_e = \sqrt{\frac{E_{frp} \cdot t_{frp}}{\sqrt{f_c}}} \qquad \text{(units: N, mm)} \tag{2.28}$$

$$\beta_w = \sqrt{\frac{2 - w_{frp} / \left(s_{frp} \cdot \sin\beta\right)}{1 + w_{frp} / \left(s_{frp} \cdot \sin\beta\right)}} \tag{2.29}$$

in which β_L is the bond length coefficient, β_w is the strip width coefficient, and L_{max} is the maximum bond length.

2.4.3.4 Monti-Liotta's model [21]

Monti and Liotta [21] proposed a set of closed form solutions for the shear strength contribution of FRP used in different retrofit techniques. For U-jacketing and full wrapping, the shear strength is obtained based on the Moersch resisting mechanism as

$$V_{frp} = 0.9 \cdot d \cdot f_{fed} \cdot 2 \cdot t_{frp} \cdot \left(\frac{w_{frp}}{s_{frp}}\right) \cdot \left(\cot\theta + \cot\alpha\right) \cdot \sin\alpha \tag{2.30}$$

For side bonding, the shear strength is obtained based on crack bridging theory as

$$V_{frp} = 0.9 \cdot d \cdot f_{fed} \cdot 2 \cdot t_{frp} \cdot \frac{\sin\alpha}{\sin\theta} \cdot \frac{w_{frp}}{s_{frp}} \tag{2.31}$$

The FRP effective bond strength, f_{fed}, is obtained in closed form, by assuming appropriate stress profiles of the FRP along the shear crack, as follows:

$$f_{fed} = \begin{cases} f_{fdd} \cdot \dfrac{z_{rid,eq}}{z} \cdot \left(1 - 0.6 \cdot \sqrt{\dfrac{L_{eq}}{z_{rid,eq}}}\right)^2 & \text{(for side bonding)} \\ f_{fdd} \cdot \left(1 - \dfrac{1}{3} \cdot \dfrac{L_e \cdot \sin\alpha}{z}\right) & \text{(for U-jacketing)} \\ f_{fdd} \cdot \left(1 - \dfrac{1}{6} \cdot \dfrac{L_e \cdot \sin\alpha}{z}\right) + \dfrac{1}{2}\left(\eta_R \cdot f_{frp,u} - f_{fdd}\right) \cdot \left(1 - \dfrac{L_e \cdot \sin\alpha}{z}\right) & \text{(for wrapping)} \end{cases} \tag{2.32}$$

where f_{fdd} is the debonding strength of the FRP sheet/strip, and L_e is the effective bond length, which are given by

$$f_{fdd} = \sqrt{0.6 \cdot \frac{E_{frp} \cdot f_{ctm} \cdot k_b}{t_{frp}}} \qquad \text{(units: N, mm)} \tag{2.33}$$

$$L_e = 0.6 \cdot \sqrt{\frac{E_{frp} \cdot t_{frp}}{\sqrt{f_{ctm} \cdot k_b}}} \qquad \text{(units: N, mm)} \tag{2.34}$$

$$k_b = \begin{cases} \sqrt{\dfrac{1.5}{1 + \left(w_{frp} / 100\text{mm}\right)}} & \text{for sheets} \\ \sqrt{\dfrac{1.5 \cdot \left(2 - w_{frp} / s_{frp}\right)}{1 + \left(w_{frp} / 100\text{mm}\right)}} & \text{for strips} \end{cases} \tag{2.35}$$

$$z_{rid,eq} = z_{rid} + L_{eq} \tag{2.36}$$

$$z_{rid} = z - L_e \cdot \sin\alpha \quad \text{and} \quad z = 0.9 \cdot d \tag{2.37}$$

$$L_{eq} = \frac{u_1}{\varepsilon_{fdd}} \cdot \sin\alpha \tag{2.38}$$

$$u_1 = 0.33 \cdot k_b \ \text{(mm)} \tag{2.39}$$

$$\eta_R = 0.2 + 1.6\frac{r_c}{b_w} \quad \text{and} \quad 0 \le \frac{r_c}{b_w} \le 0.5 \tag{2.40}$$

in which r_c is the corner rounding radius, f_{ctm} is the tensile strength of concrete, k_b is the covering scale/coefficient, and the quantity w_{frp} for sheets is defined as

$$w_{frp} = \min\left(0.9d, h\right) \cdot \sin\left(\theta + \alpha\right) / \sin\theta \tag{2.41}$$

3. PROPOSED MODEL

This study proposes a new model for evaluating the contribution to the shear strength of RC members due to FRP retrofit. This model is based on an FRP stress distribution along the shear crack similar to the one adopted by the Monti-Liotta's model [21]. The proposed model presents the following major differences when compared with the Monti-Liotta's model:

(1) For side bonding retrofit, this model accounts for the shear strength contribution due to the portion of FRP for which the available bonding length is smaller than the effective bond length after debonding is initiated. In addition, this model differentiates the FRP shear strength contributions for cases in which the available bond length is higher or lower than the effective bond length. Finally, the FRP shear strength contribution is evaluated as the minimum between the contributions computed using the crack bridging theory and the Moersch truss analogy.

(2) For U-jacketing retrofit, the proposed model takes into consideration the two possible values of maximum available bond length corresponding to the location where the debonding of the FRP starts.

(3) For wrapping retrofit, this model does not consider the effect of FRP debonding.

The proposed model estimates the maximum contribution of the FRP strips/sheets as a function of FRP stress profile for the following three FRP shear strengthening techniques: (a) side bonding, (b) U-jacketing, and (c) wrapping. The effective stress carried by the FRP sheet/strip externally bonded to the RC beam depends on the properties of the retrofitted RC member and the FRP shear retrofit. The following hypotheses are made:

- the shear cracks are evenly distributed along the beam axis;

- the shear cracks are linear and inclined at a constant angle of θ with respect to the longitudinal axis of the beam;
- the FRP strips/sheets have only axial stiffness and the fibers are oriented at an angle α with respect to the longitudinal axis of the beam;
- at the ultimate limit state, the depth of the crack is equal to $z = 0.9 \cdot d$.

In case of U-jacketing and wrapping retrofit, the FRP shear strength contribution is given by the Moersch truss analogy. However, in case of side bonding, the FRP resistance mechanism is controlled by crack bridging theory or Moersch truss analogy. Thus, the FRP shear strength contribution for side bonding retrofit is taken as the minimum value given by crack bridging and Moersch truss analogy. The FRP shear strength contribution is given as

$$V_{frp} = \begin{cases} 0.9 \cdot d \cdot b_w \cdot \rho_{frp} \cdot f_{frp,e} \cdot \left(\cot\theta + \cot\alpha\right) \cdot \sin\alpha & \text{Moersch truss analogy} \\ 0.9 \cdot d \cdot f_{frp,e} \cdot 2t_f \cdot \dfrac{\sin\alpha}{\sin\theta} \cdot \dfrac{w_f}{s_f} & \text{Crack bridging theory} \end{cases} \tag{3.1}$$

$$f_{frp,e} = \frac{\int_0^{L_f} \sigma_{frp}\left(L_a(x), L_e, f_{fdd}(L), u(x,u_1), f_{frp,u}, \text{geom}\right) \cdot \mathrm{d}x}{L_f} \tag{3.2}$$

$$L_f = \frac{0.9 \cdot d}{\sin\theta} \tag{3.3}$$

where σ_{frp} is the stress carried by the FRP at a given coordinate *x* along the shear crack. This stress is a function of the available bond length $L_a(x)$, effective length L_e, FRP debonding strength $f_{fdd}(L)$, FRP slip *u*, ultimate tensile strength of the FRP $f_{frp,u}$, as well as geometry of the beam cross section and type of shear retrofit (geom). Figure 3-1 provides the geometric properties for the proposed model.

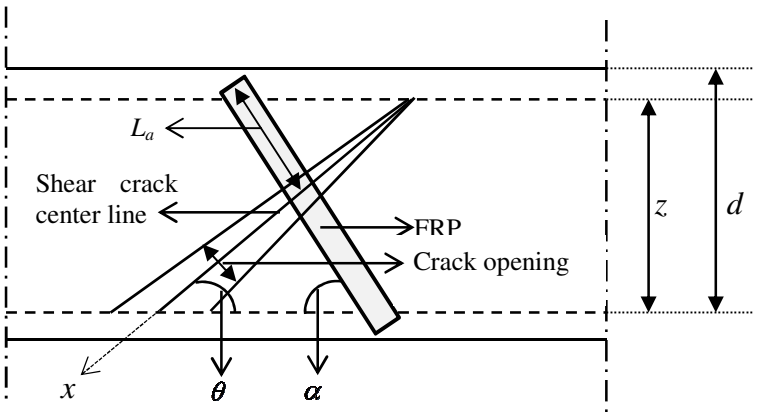

Figure 3-1: Notation used for the geometric properties

The computation of $f_{frp,e}$, depends on the three following aspects:

a) the generalized failure criterion of the FRP sheet/strip bonded to the concrete;

b) the boundary conditions of the problem, which determine the available bond length for different geometric configuration of the shear retrofit;

c) the FRP stress-slip relation along a shear crack.

3.1 Generalized failure criterion

The generalized failure criterion for a strip/sheet of FRP externally bonded to concrete provides two quantities: (a) the FRP debonding strength, f_{fdd}, which represents the maximum stress that a FRP sheet/strip can carry on an uncracked concrete surface before the start of debonding; and (b) the effective bond length, L_e, which is the anchorage length beyond which no increase in the stress carried by the FRP is obtained.

The failure criterion adopted in this study is given by Monti et al. [22]. Figure 3-2 shows the force-slip relation for a FRP strip/sheet externally bonded to concrete. The figure indicates three characteristic points: point 1 separates the linear and the non-linear behavior and indicates the starting of interface cracking; point 2 corresponds to the starting of debonding when the pulled

end slip reaches the ultimate slip, u_1, and the maximum pulling force, F_{max} is achieved here and the bond length is termed as effective bond length, L_e; point 3 corresponds to the continuation of debonding into the anchorage length which happens at a constant value of pulling force equal to F_{max} until the remaining available anchorage length is larger or equal than the effective length.

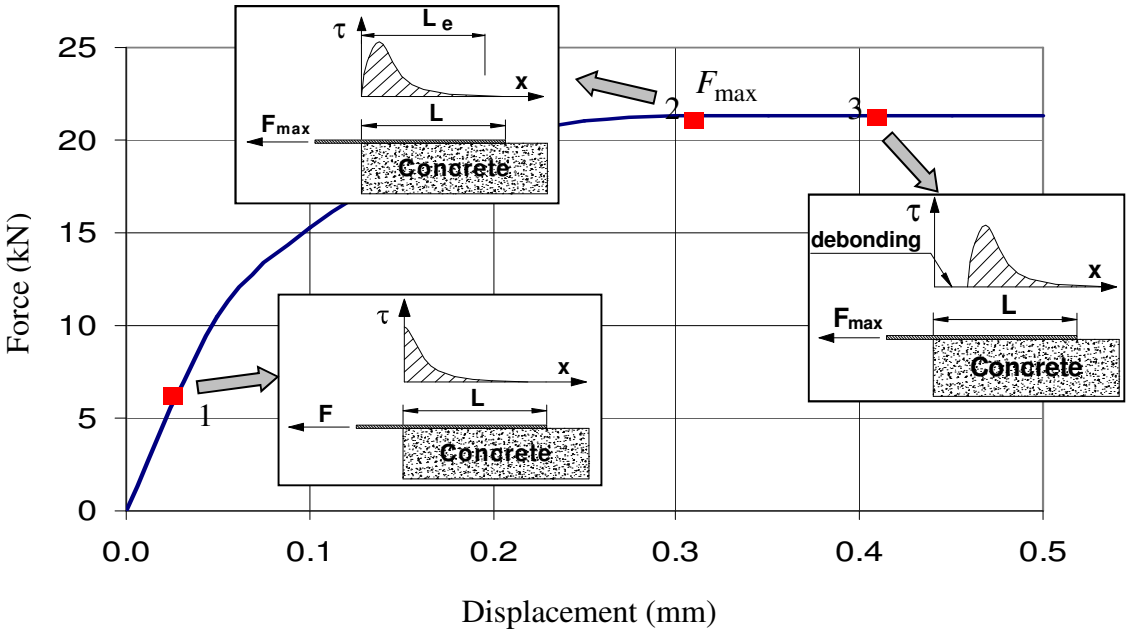

Figure 3-2: Force slip relation for FRP bonded on concrete (adapted from [22])

The FRP debonding strength and the effective bond length adopted from the Monti-Renzelli model [22] are given as,

$$f_{fdd}(L) = \beta(L) \cdot \sigma_{max} \tag{3.4}$$

and

$$L_e = \sqrt{\frac{E_{frp} \cdot t_{frp}}{\sqrt{4 \cdot \tau_{max}}}} \qquad \text{(units: N, mm)} \tag{3.5}$$

respectively, where

$$\sigma_{max} = \sqrt{\frac{E_{frp} \cdot \tau_{max}}{3 \cdot t_{frp}}} \qquad \text{(units: N, mm)} \tag{3.6}$$

$$\beta(L) = \begin{cases} \sin\left(\frac{\pi}{2} \cdot \frac{L}{L_e}\right) & \text{for } L < L_e \\ 1 & \text{for } L \geq L_e \end{cases} \tag{3.7}$$

and

$$\tau_{max} = k_b \cdot 1.8 \cdot f_{ctm} \tag{3.8}$$

in which τ_{max} is the peak bond stress, L is the available bond length, and f_{ctm} is the concrete tensile strength, and

$$k_b = \begin{cases} \sqrt{\frac{1.5\left(2 - w_{frp} / s_{frp}\right)}{1 + w_{frp} / 100}} & \text{for strips} \\ \sqrt{\frac{1.5}{1 + w_{frp} / 100}} & \text{for sheets} \end{cases} \qquad \text{(units: mm)} \tag{3.9}$$

For FRP sheets, the w_{frp} is computed as

$$w_{frp} = \frac{\min\left(0.9 \cdot d, h_w\right) \cdot \sin\left(\theta + \alpha\right)}{\sin\theta} \qquad \text{(units: mm)} \tag{3.10}$$

3.2 Boundary conditions

The boundary conditions in the problem determine the available bond lengths, $L(x)$, on both sides of the shear crack and are defined by the FRP strengthening technique. Figure 3-3 describes the boundary conditions for the three considered strengthening techniques adopted: side bonding (S), U-jacketing (U), and wrapping (W).

The available bond length is given as [21]

$$L(x)=\begin{cases} L_S(x)=\min\left\{L_{top}(x),L_{bot}(x)\right\} & \text{for side bonding} \\ L_U(x)=L_{top}(x) & \text{for U-jacketing} \\ L_W(x)=\max\left\{L_{top}(x),L_{bot}(x)\right\} & \text{for wrapping} \end{cases} \tag{3.11}$$

where $L_S(x)$ is the available bond length for side bonding, $L_U(x)$ is the available bond length for U-jacketing, and $L_W(x)$ is the available bond length for wrapping, and are defined as

$$L_S(x)=\begin{cases} x\cdot\dfrac{\sin\theta}{\sin\alpha} & \text{for } 0\le x\le\dfrac{z}{2\cdot\sin\theta} \\ \dfrac{z}{\sin\alpha}-x\cdot\dfrac{\sin\theta}{\sin\alpha} & \text{for } \dfrac{z}{2\cdot\sin\theta}\le x\le\dfrac{z}{\sin\theta} \end{cases} \tag{3.12}$$

$$L_U(x)=x\cdot\frac{\sin\theta}{\sin\alpha} \quad \text{for } 0\le x\le\frac{z}{\sin\theta} \tag{3.13}$$

$$L_W(x)=\begin{cases} \dfrac{z}{\sin\alpha}-x\cdot\dfrac{\sin\theta}{\sin\alpha} & \text{for } 0\le x\le\dfrac{z}{2\cdot\sin\theta} \\ x\cdot\dfrac{\sin\theta}{\sin\alpha} & \text{for } \dfrac{z}{2\cdot\sin\theta}\le x\le\dfrac{z}{\sin\theta} \end{cases} \tag{3.14}$$

3.3 Stress-slip constitutive law

The generalized stress slip constitutive law for FRP strip/sheet externally bonded to the concrete is given as

$$\sigma_{frp}(u)=\begin{cases} f_{fdd}\cdot\sin\left(\dfrac{\pi}{2}\cdot\dfrac{u}{\mathrm{u}_1}\right) & \text{if } u\le \mathrm{u}_1 \\ f_{fdd} & \text{if } \mathrm{u}_1\le u\le u_d \\ f_{fdd}\cdot\cos\left(\dfrac{\pi}{2}\cdot\dfrac{u-u_d}{\mathrm{u}_1}\right) & \text{if } u_d\le u\le u_u \\ 0 & \text{if } u>u_u \end{cases} \tag{3.15}$$

where u_1 is the pulled end slip at the start of debonding, u_d is the pulled end slip at complete debonding over the length $L-L_e$, and u_d is the pulled end slip at complete debonding over the entire length *L*.

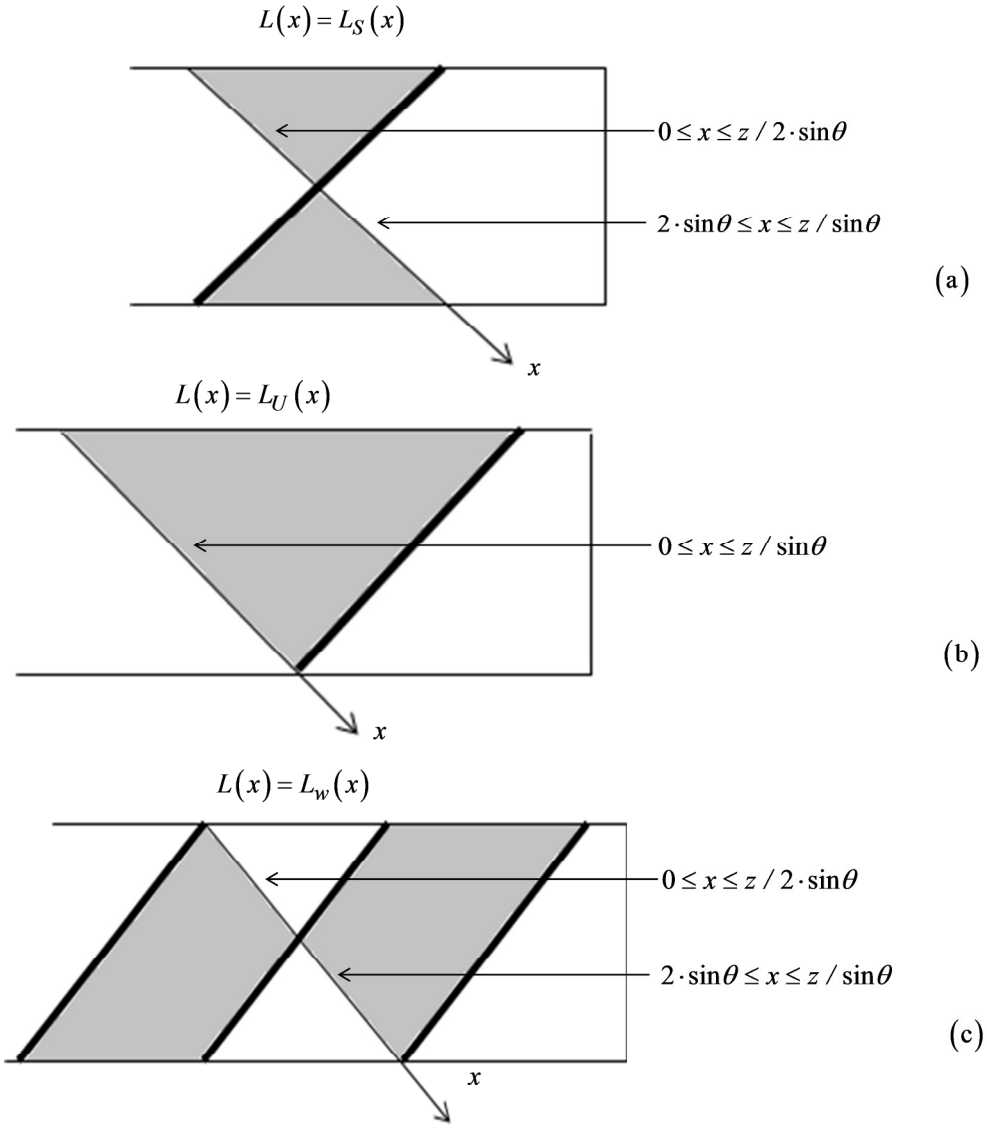

Figure 3-3: Boundary conditions for: (a) side bonding; (b) U-jacketing; (c) wrapping

3.4 Calculation of $f_{frp,e}$ for side bonding

The collapse mechanism of FRP sheets/strips externally bonded to the RC beams in shear is mainly controlled by debonding. The FRP stress profile along the crack is obtained by adopting the stress-slip law discussed in Section 3.3. The stress slip law is approximated by a sinusoidal curve till the point of starting of the debonding and a straight line indicating the progress of debonding. The maximum available bond length marks the onset of debonding. The FRP stress profile is identified for three different cases of maximum available anchorage length and effective length.

Case 1: $(L_a)_{max} \geq L_e$

The FRP stress profile for this case is described by three different components, as shown in Figure 3-6.

(1) The first component corresponds to a sinusoidal increase from zero stress at the top of the shear crack where the FRP concrete slip and the stress in the FRP are equal to zero to the point of maximum anchorage length where $\sigma = \sigma_{max}$ (in which σ_{max} corresponds to the maximum FRP debonding strength). At this point the slip reaches u_1, indicating starting of debonding, and the available bond length is the maximum available bond length.

(2) The second component corresponds to a constant stress value $\sigma = \sigma_{max}$ between the point with maximum available bond length and the point where the FRP debonding has progressed until $L_a(x) - \Delta L(x) \geq L_e$.

(3) The third component corresponds to a sinusoidal decrease in stress value until full debonding is reached. $\Delta L(x)$ is the decrease in the available bond length due to debonding of the FRP and is given by Equation (3.15). However, taking into consideration the actual collaboration between

the adhesion fibres, only a portion of the third component can be accounted for the calculation of the effective stress carried by the FRP sheet/strip. This portion is assumed equal to 0.5 in this study. The decrease in available bond length (which corresponds to the debonded length of FRP) is given by

$$\Delta L(x) = \frac{\Delta u(x)}{\varepsilon} = \frac{\Delta u(x) \cdot E_{frp}}{\sigma_{max}} \tag{3.15}$$

where (see Figure 3-5)

$$\Delta u(x) = u(x) - u_1 \tag{3.15}$$

Thus the stress carried by the FRP is given as

$$\sigma_{FRP}(x) = \begin{cases} \sigma_{max} \cdot \sin\left[\frac{\pi}{2} \cdot \frac{u(x)}{u_1}\right] & \text{for } x \le x' \\ \sigma_{max} & \text{for } x' \le x \le x'' \\ \frac{\sigma_{max}}{2} \cdot \sin\left[\frac{\pi}{2} \cdot \frac{L_a(x) - \Delta L(x)}{L_e}\right] & \text{for } x'' \le x \le x''' \\ 0 & \text{for } x \ge x''' \end{cases} \tag{3.15}$$

where

$$\begin{aligned} &x' \rightarrow L_a(x') = (L_a)_{max} \\ &x'' \rightarrow L_a(x'') - \Delta L(x'') = L_e \\ &x''' \rightarrow L_a(x''') = \Delta L(x''') \end{aligned} \tag{3.15}$$

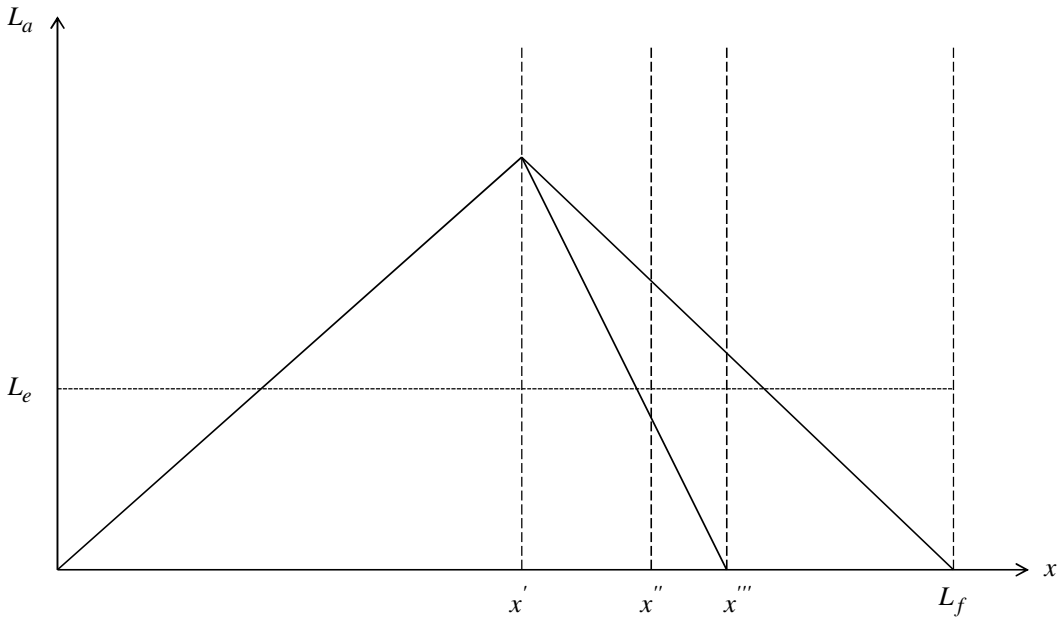

Figure 3-4: Side bonding: bond length for $(L_a)_{max} \geq L_e$

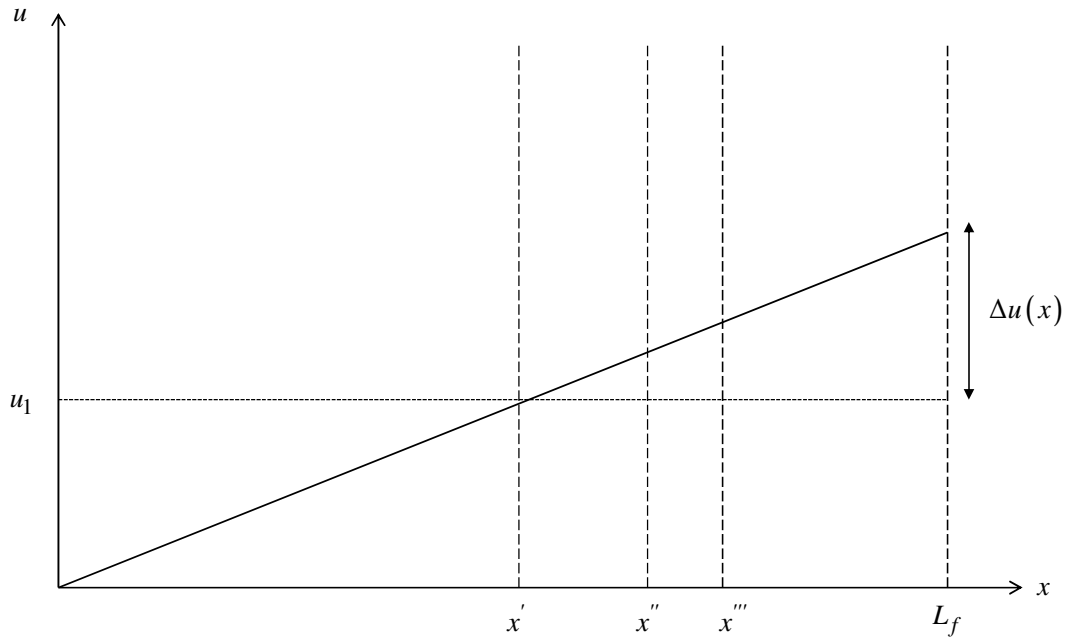

Figure 3-5: Side bonding: pulled end slip for $(L_a)_{max} \geq L_e$

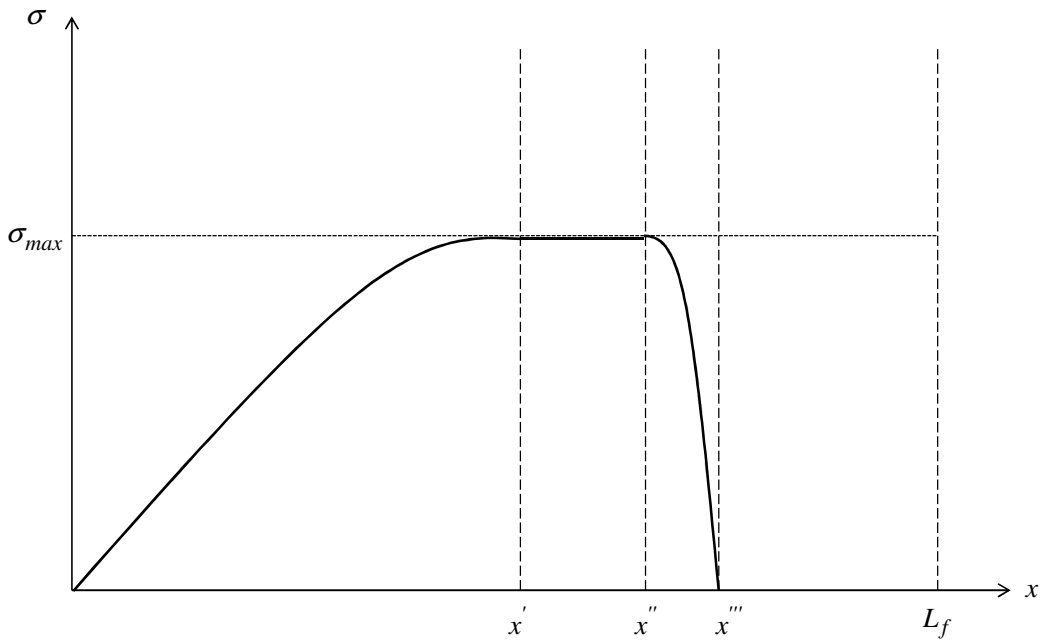

Figure 3-6: Side Bonding: FRP stress profile for $(L_a)_{max} \geq L_e$

Case 2: $(L_a)_{max} < L_e$

The FRP stress profile for this case is defined by two different components, as shown in Figure 3-9. The first component corresponds to a sinusoidal increase to the point to maximum anchorage length where $\sigma = \overline{\sigma}_{max}$. The second component corresponds to a sinusoidal decrease in stress value until full debonding.

Thus, the stress carried by the FRP is given by

$$\sigma_{FRP}(x) = \begin{cases} \overline{\sigma}_{max} \cdot \sin\left[\frac{\pi}{2} \cdot \frac{u(x)}{u_1}\right] & \text{for } x \leq x' \\ \frac{\overline{\sigma}_{max}}{2} \cdot \sin\left[\frac{\pi}{2} \cdot \frac{L_a(x) - \Delta L(x)}{L_e}\right] & \text{for } x' \leq x \leq x''' \\ 0 & \text{for } x \geq x''' \end{cases} \tag{3.16}$$

where

$$\overline{\sigma}_{max} = \sigma_{max} \cdot \sin\left(\frac{\pi}{2} \cdot \frac{(L_a)_{max}}{L_e}\right) \tag{3.17}$$

$$\bar{u}_1 = \mathrm{u}_1 \cdot \sin\left(\frac{\pi}{2} \cdot \frac{(L_a)_{max}}{L_e}\right) \tag{3.18}$$

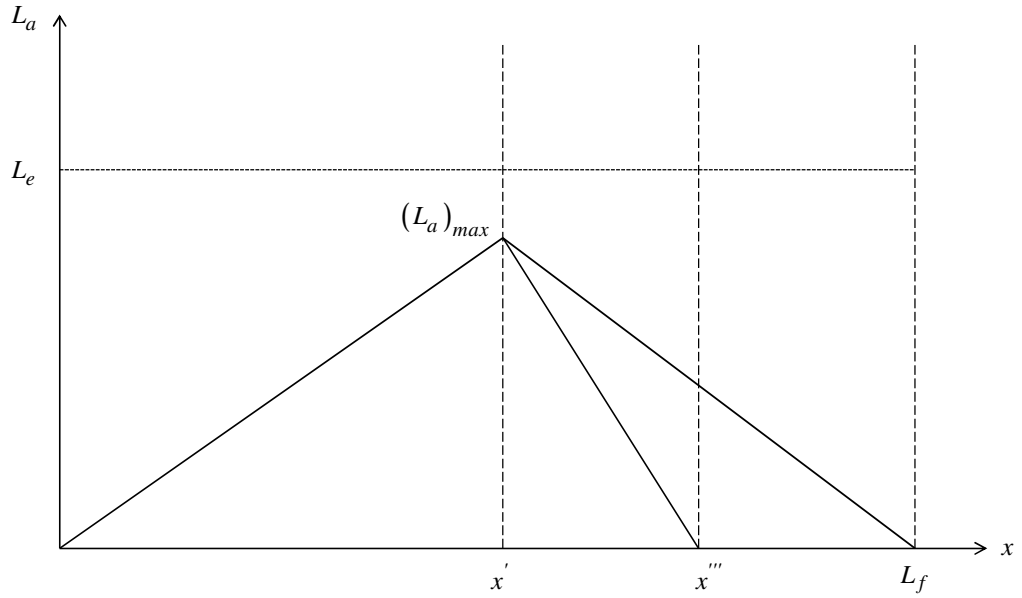

Figure 3-7: Side Bonding: bond length for $(L_a)_{max} < L_e$

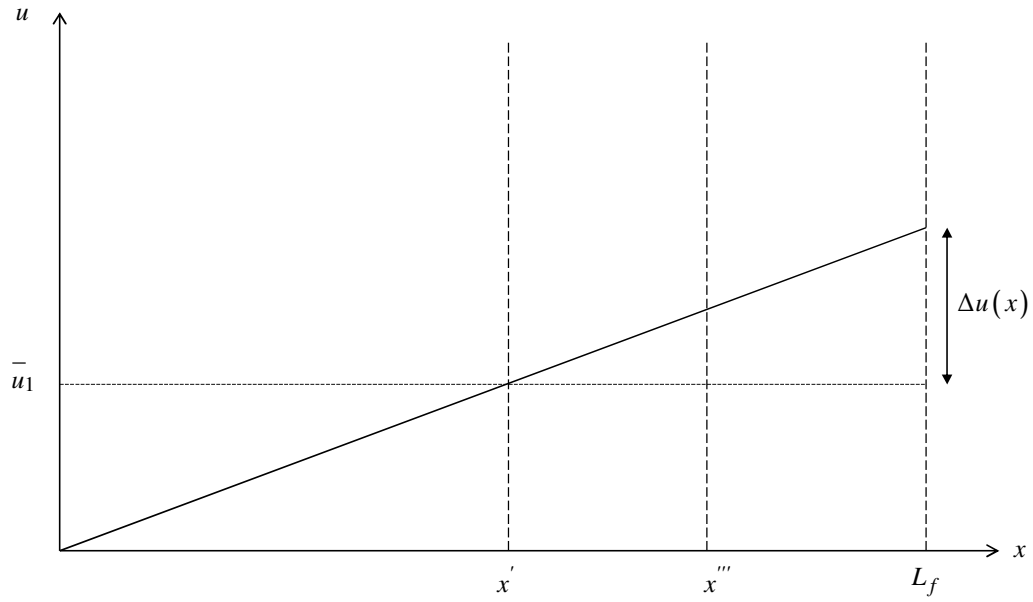

Figure 3-8: Side Bonding: pulled end slip for $(L_a)_{max} < L_e$

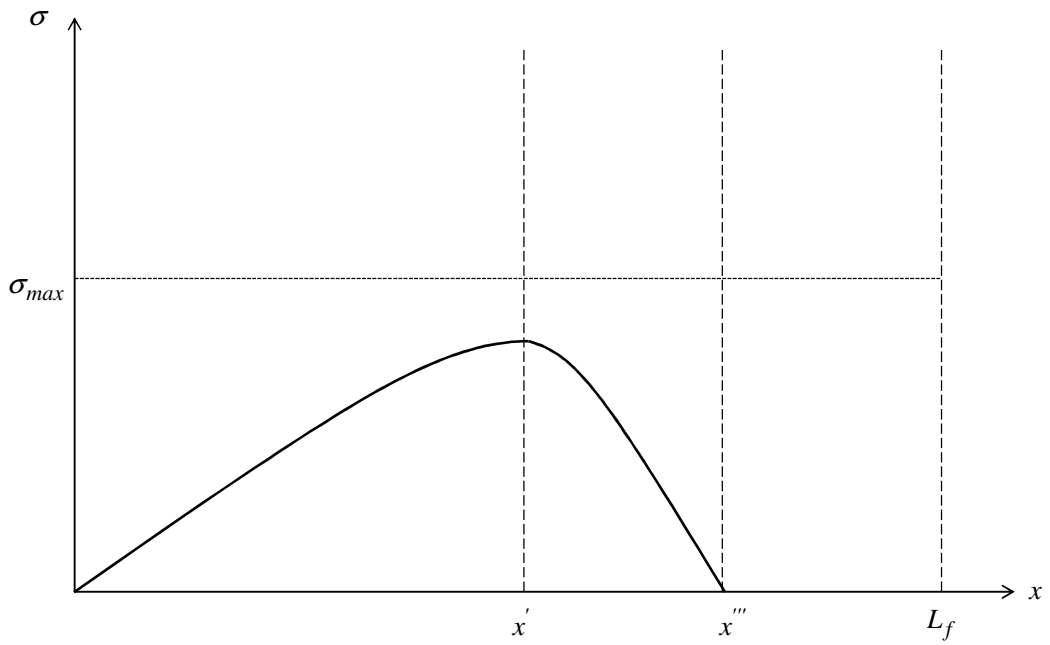

Figure 3-9: Side Bonding: FRP stress profile for $(L_a)_{max} < L_e$

Case 3: $(L_a)_{max} = L_e$

In this case $\overline{\sigma}_{max} = \sigma_{max}$, $\overline{u}_1 = \mathrm{u}_1$, $x' \equiv x''$ and the FRP stress profile is given by Figure 3-12.

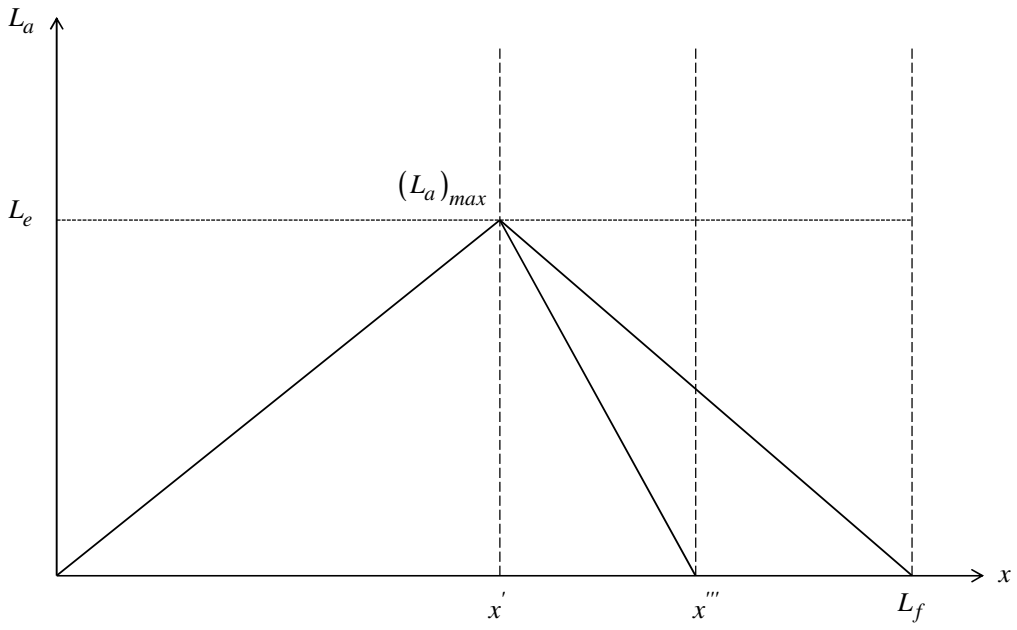

Figure 3-10: Side bonding: bond length for $(L_a)_{max} = L_e$

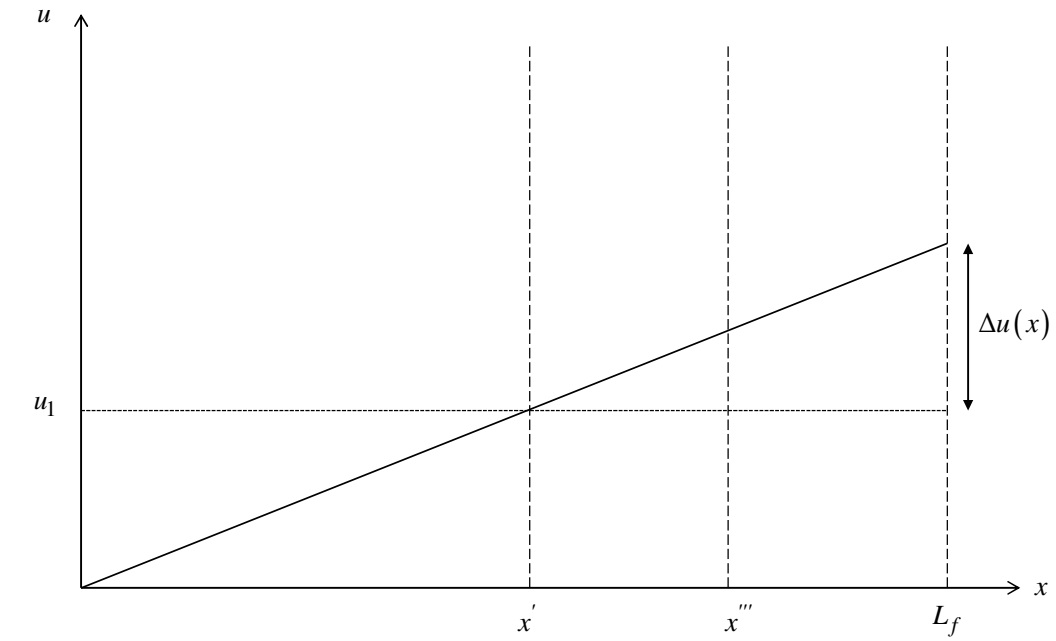

Figure 3-11: Side bonding: pulled end slip for $(L_a)_{max} = L_e$

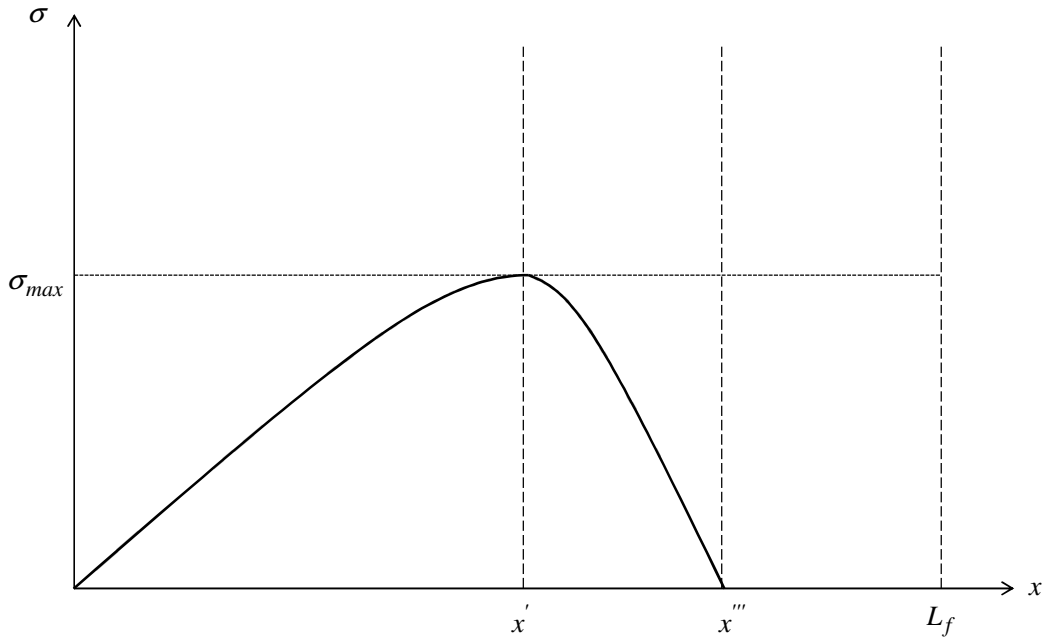

Figure 3-12: Side bonding: FRP stress profile for $(L_a)_{max} = L_e$

3.5 Calculation of $f_{frp,e}$ for U-jacketing

For U-jacketing, the debonding occurs at the free end of the FRP and, thus, the available bond lengths are significantly larger than for side bonding. The maximum available bond length indicates the maximum stress carried by the FRP. The FRP stress distribution for U-jacketing is given for two cases.

Case 1: $\left(L_a\right)_{max} \geq L_e$

The stresses in the FRP continue to increase till the debonding in the FRP does not reduce the available bond length less than the effective bond length. Thus the FRP stress profile represents a sinusoidal curve increasing up to the point of maximum available bond length. The maximum available bond length is computed in correspondence of the maximum between points x' and $\bar{x}$, which are defined by the following relations. The maximum between x' and $\bar{x}$ corresponds to the location where the debonding of the FRP starts. When the debonding starts from the farther end of the corner of the FRP, a smaller value of $\bar{x}$ is obtained. Further, when the FRP sheet/strip is wrapped around a corner, the maximum stress carried in the FRP is the minimum between the maximum debonding strength σ_{max} (see Equation (3.20)) and a fraction η_R of the tensile strength of the FRP (see Equation (2.40)). Thus the effective stress carried by the FRP can be computed in closed form as,

$$f_{frp,e} = \sigma'_{max} \cdot \left(1 - \frac{\pi - 2}{\pi} \cdot \frac{\max\left(x', \bar{x}\right)}{L_f} \right) \tag{3.19}$$

in which

$$\sigma'_{max} = \min\left(\sigma_{max}, \eta_R \cdot f_{frp,u}\right) \tag{3.20}$$

$$x' = L_e \frac{\sin\alpha}{\sin\theta} \tag{3.21}$$

$$\bar{x} = \frac{u_1}{u_{max}} \cdot L_f \tag{3.22}$$

$$u_{max} = u_1 + \frac{\sigma'_{max}}{E_{frp}} \cdot \left((L_a)_{max} - L_e \right) \tag{3.23}$$

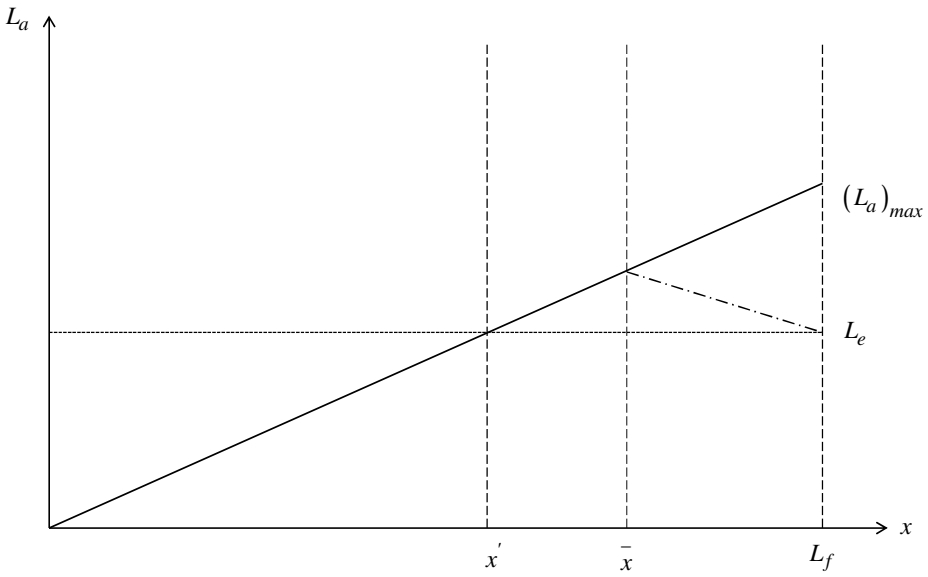

Figure 3-13: U-jacketing: bond length for $(L_a)_{max} \geq L_e$ and $\bar{x} \geq x'$

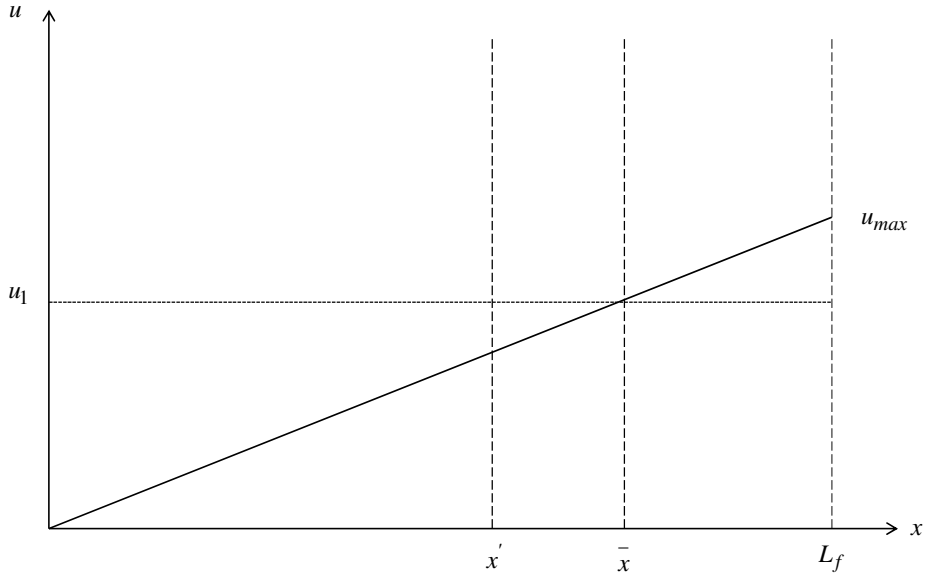

Figure 3-14: U-jacketing: pulled end slip for $(L_a)_{max} \geq L_e$ and $\bar{x} \geq x'$

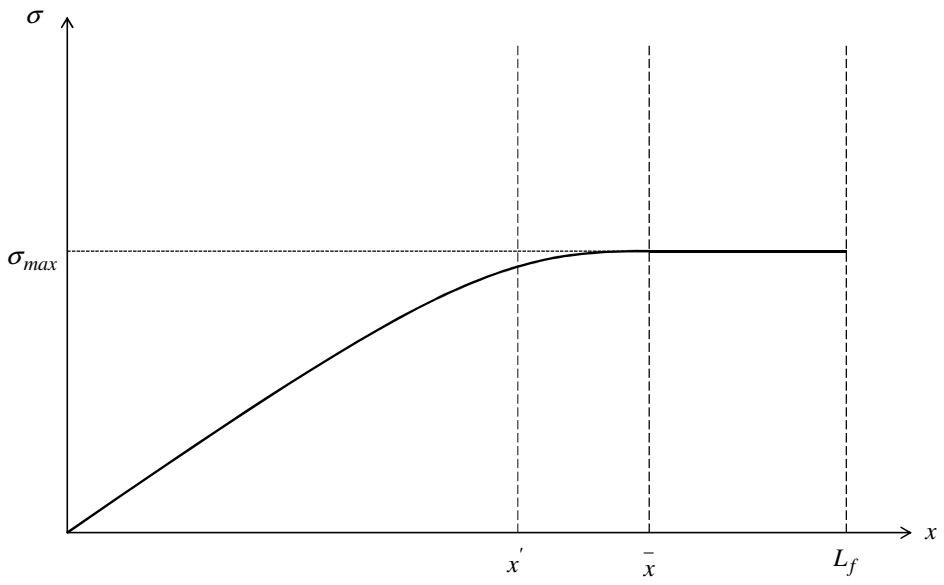

Figure 3-15: U-jacketing: FRP stress profile for $(L_a)_{max} \geq L_e$ and $\bar{x} \geq x'$

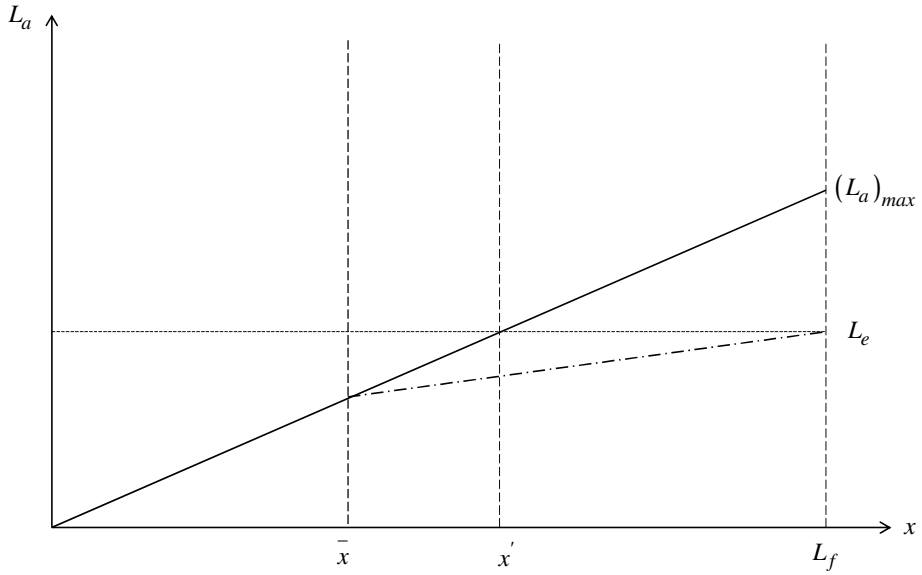

Figure 3-16: U-jacketing: bond length for $(L_a)_{max} \geq L_e$ and $\bar{x} < x'$

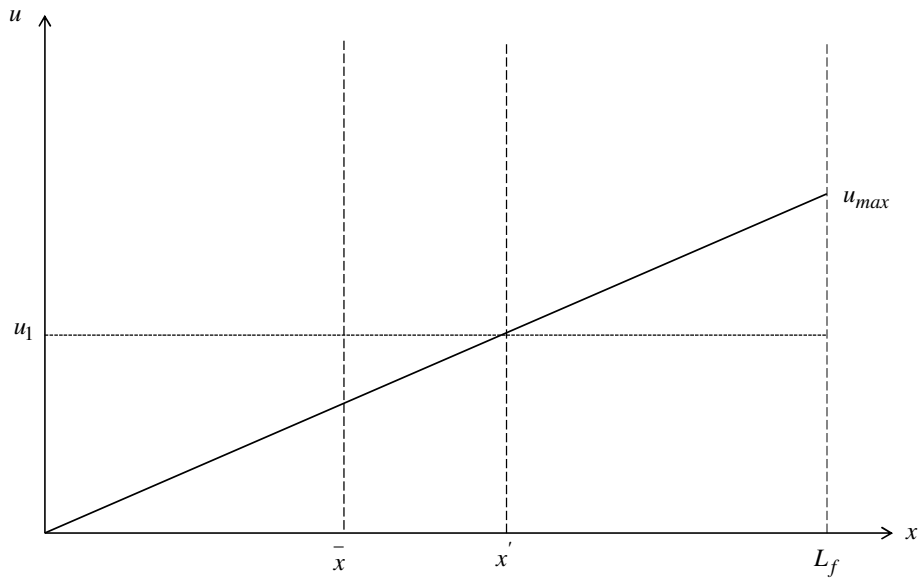

Figure 3-17: U-jacketing: pulled end slip for $(L_a)_{max} \geq L_e$ and $\bar{x} < x'$

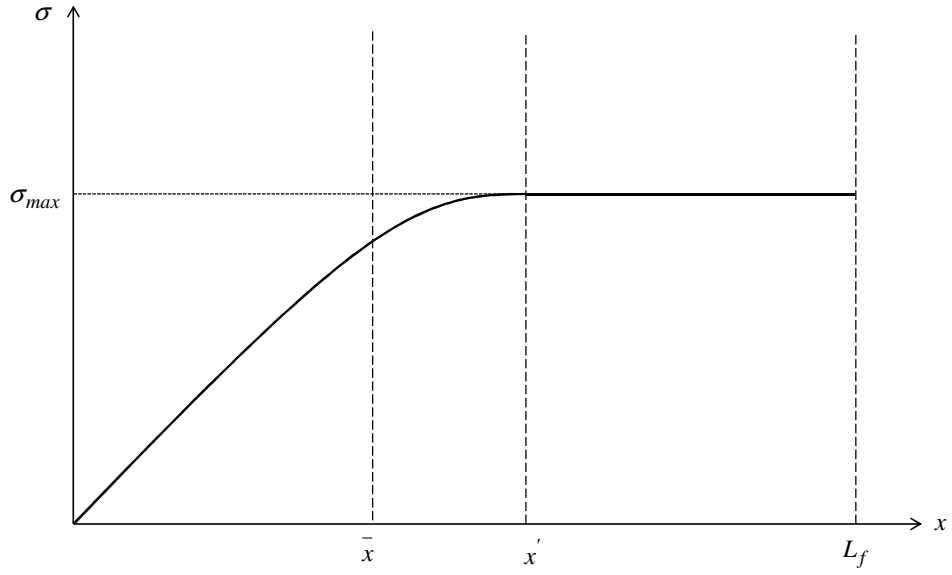

Figure 3-18: U-jacketing: FRP stress profile for $(L_a)_{max} \geq L_e$ and $\bar{x} < x'$

Case 2: $(L_a)_{max} < L_e$

The FRP stress profile is a single sinusoidal curve growing to the point maximum available bond length, where the FRP reaches maximum stress. The effective stress carried by the FRP is computed in closed form as

$$f_{frp,e} = \frac{2}{\pi} \cdot \min\left[\sigma_{max} \cdot \sin\left(\frac{\pi}{2} \cdot \frac{(L_a)_{max}}{L_e} \right), \eta_R \cdot f_{frp,u} \right] \tag{3.24}$$

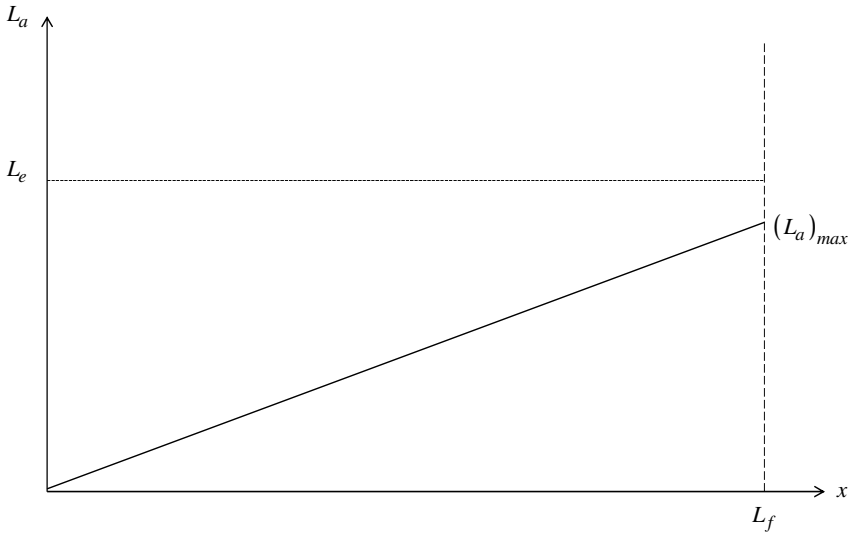

Figure 3-19: U-jacketing: bond length for $(L_a)_{max} < L_e$

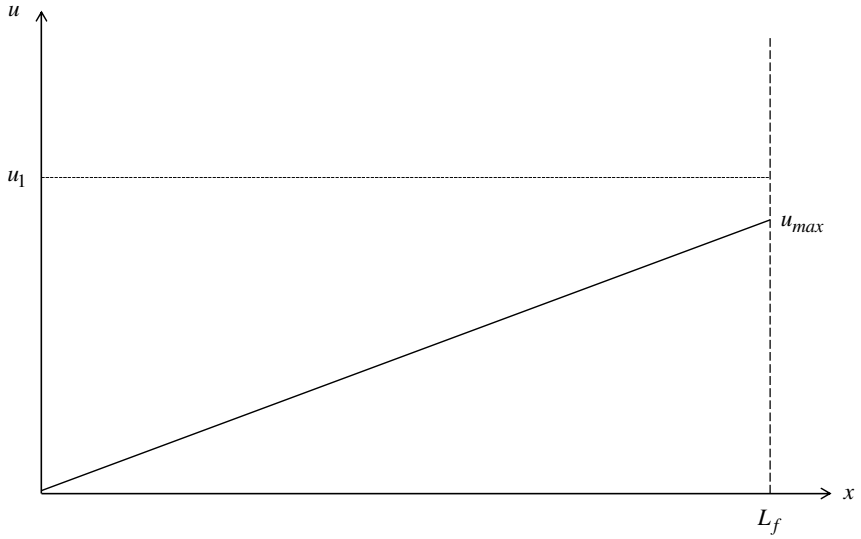

Figure 3-20: U-jacketing: pulled end slip for $(L_a)_{max} < L_e$

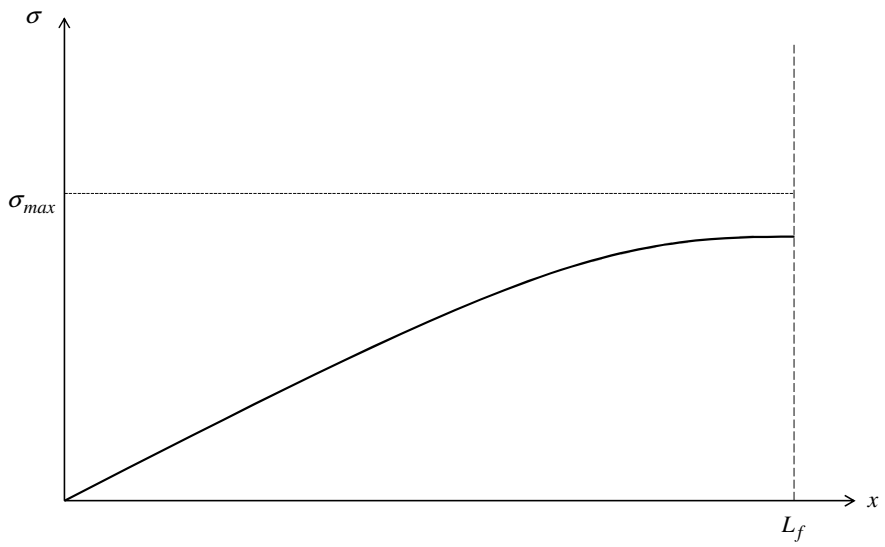

Figure 3-21: U-jacketing: FRP stress profile for $(L_a)_{max} < L_e$

3.6 Calculation of $f_{frp,e}$ for wrapping

The collapse mechanism of beams retrofitted with FRP wrapped is a combination of the tensile rupture of the FRP and the degradation of the strength of concrete. Neglecting the effect of FRP debonding, the FRP stress profile represents a straight line increasing till it reaches the ultimate tensile strength. The effective stress is given by

$$f_{frp,e} = \frac{1}{2} \cdot \left(\eta_R \cdot f_{frp,u} \right) \tag{3.25}$$

where η_R is given in Equation (2.40).

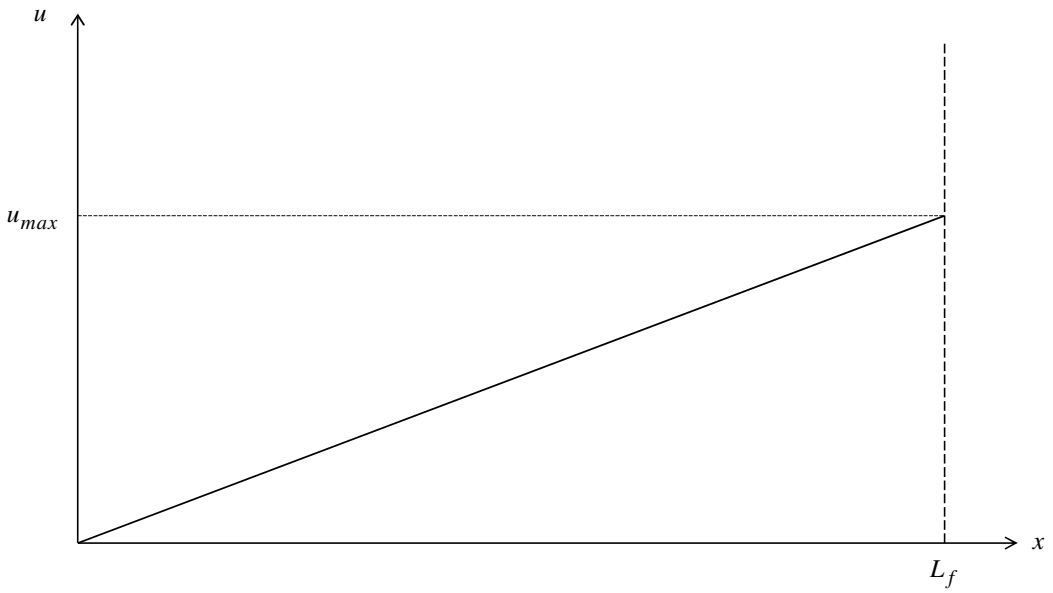

Figure 3-22: Pulled end slip for FRP wrapping

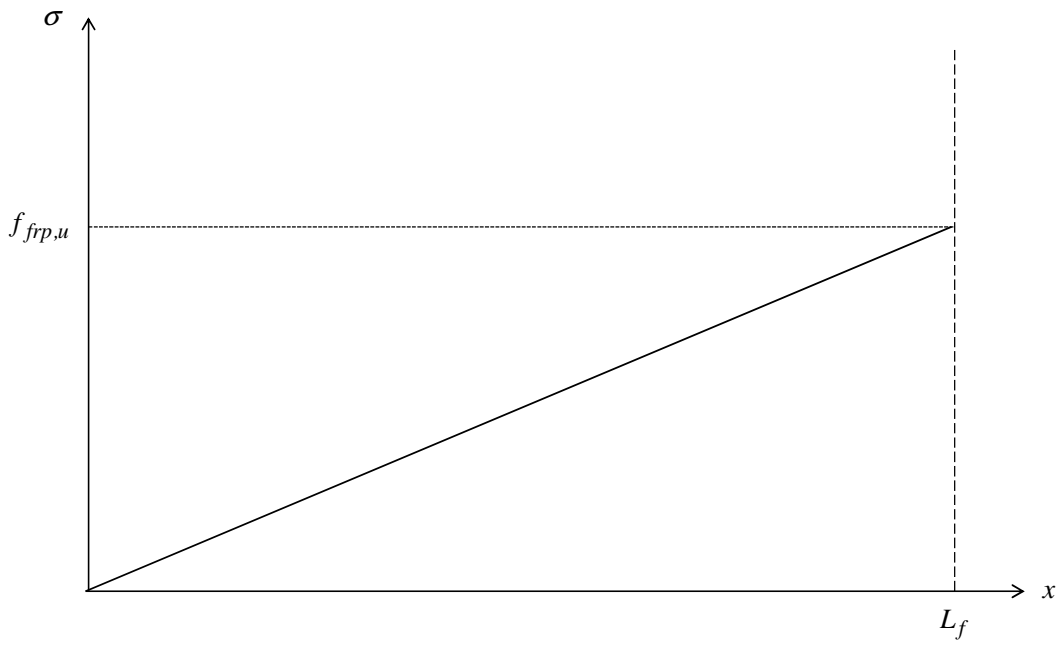

Figure 3-23: FRP stress profile for FRP wrapping

3.7 Comparison of results for proposed model and existing models from literature

Several authors [18]-[21],[33]-[45] have experimentally studied the effects of FRP shear retrofit in RC beams. The data from the referenced papers have been used in this study to compute the FRP shear strength contribution estimated using the newly proposed model and to compare these results with those obtained using other models discussed in the literature review. The experimental data used for this comparison was limited to beams satisfying the condition $a/d \geq 2.5$ and failing by pure shear.

The total number of beams with FRP shear retrofit used for this comparison is 57, among which 25 beams are with FRP side bonding, 10 beams with FRP U-jacketing, and 22 beams with FRP wrapping. The different models were compared based on the relative percentage of error (ε_{theo}), and the ratio of theoretical to experimental FRP shear strength contribution (R_{theo}), which are defined as

$$\varepsilon_{theo} = 100 \cdot \frac{V_{frp,theo} - V_{frp,exp}}{V_{frp,exp}} \tag{3.26}$$

$$R_{theo} = \frac{V_{frp,theo}}{V_{frp,exp}} \tag{3.27}$$

The cross sectional details and material properties of all the RC beams considered in this study are summarized in Table 3-1. Table 3-2 provides the FRP retrofit details and the properties of the FRP. Table 3-3 provides the values of the computed V_{frp}, ε_{theo}, and R_{theo} for the all the considered RC beams, relative to the following models for FRP shear strengthening: (1) ACI, (2) Triantafillou, (3) Cheng-Teng (4) Monti-Liotta, and (5) proposed model.

The following results were obtained:

- Considering all three retrofit techniques, the proposed model gave an average ε_{theo} of 21.76%, with a standard deviation of 46.13%. The average value of R_{theo} is 1.22 and the corresponding standard deviation is 0.46.
- In case of side bonding retrofit, the average ε_{theo} is 9.27%, and the corresponding standard deviation is 27.36%, and the average value of R_{theo} is 1.09, and the corresponding standard deviation is 0.27.
- In case of U-jacketing retrofit, the average ε_{theo} is 69.52%, and the corresponding standard deviation is 42.66%, and the average value of R_{theo} is 1.70, and the corresponding standard deviation is 0.43.
- In case of wrapping retrofit, the average ε_{theo} is 14.65%, and the corresponding standard deviation is 52.31%, and the average value of R_{theo} is 1.15, and the corresponding standard deviation is 0.27.

It is observed that the newly proposed model is overall in better agreement with the experimental results when compared to the other considered models in terms of ε_{theo} and R_{theo}. The agreement of the proposed model with the experimental results is excellent for side bonding retrofit, fair for U-jacketing, and good for wrapping. . For U-jacketing retrofit, the proposed model gave the smallest standard deviation of ε_{theo} and R_{theo} when compared with the other considered models. However, the mean error of the proposed model is larger than all other models, with the exception of the Monti-Liotta's model. In the case of wrapping retrofit, the proposed model is better agreement with the experimental results when compared to the other models considered in this research, with the exception of the Triantafillou's model, which provides the best agreement with the experimental results.

Figure 3-24 graphically reproduces the results for the FRP shear strength increase provided in Table 3-3. The experimental and theoretical shear strength increases are represented on the horizontal and vertical axes, respectively. The dashed line in the Figure 3-24 represents the perfect agreement between computed and experimental results, i.e., $R_{theo} = 1$.

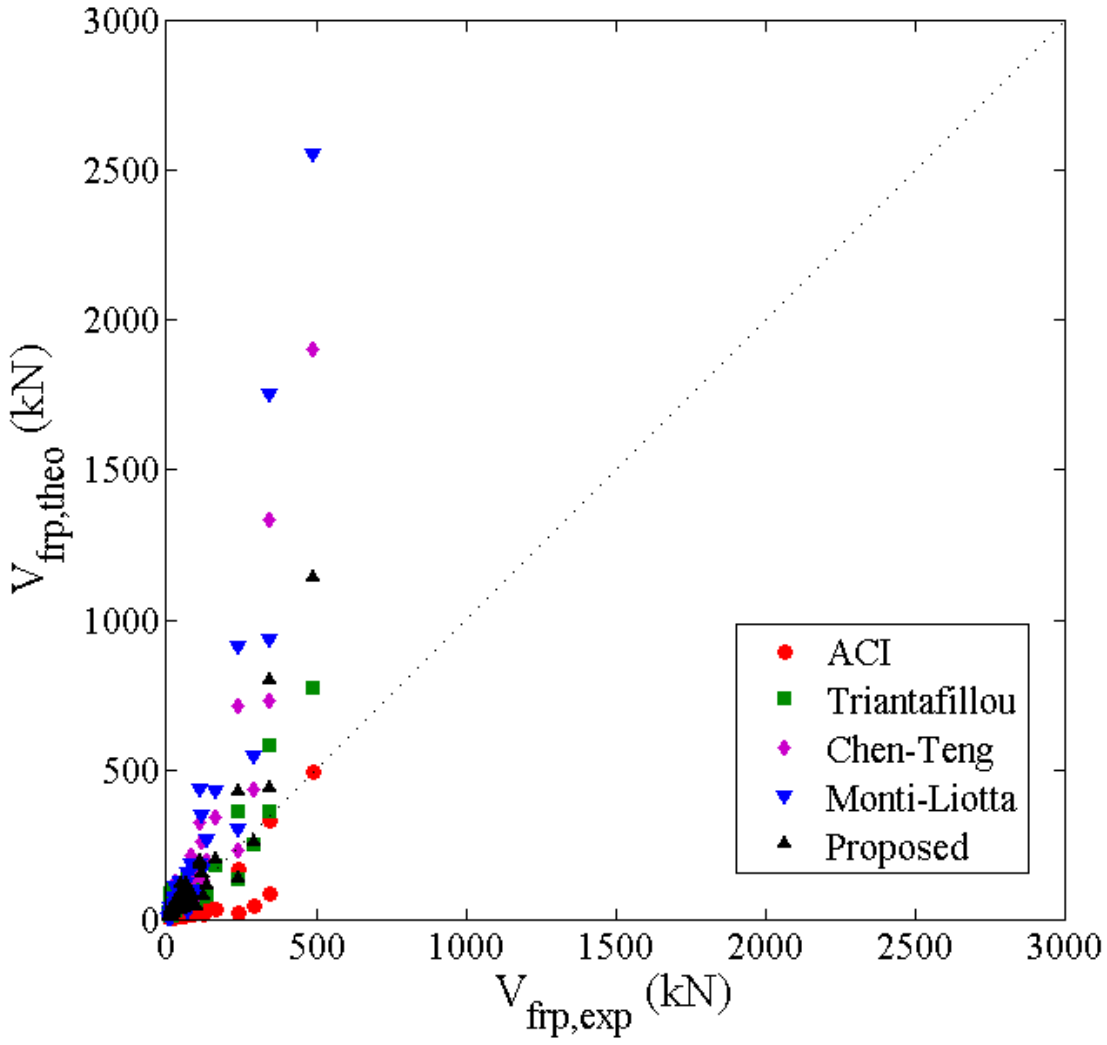

Figure 3-24: Comparison between theoretical and experimental results of RC beams with a/d ≥ 2.5 and pure shear failure: FRP shear strength contribution

Table 3-1: Cross sectional details and material properties

		b_w (mm)	d (mm)	a/d	f_c (MPa)	A_{sb} $(mm)^2$	A_{st} $(mm)^2$	A_s $(mm)^2$	f_y (MPa)
Triantafillou [18]	Control S1 S1-45 S2 S2-45 S3 S3-45	70	100	3.20	30	100.5	0	0	500
Al Sulaimani [24]	Control SO WO JO	150	113	3.50	37.7	339.3	56.5	56.5	450
Zhang and Teng [34]	Control Z6-90	152.4	194.5	2.74	43.8	427.5	63.33	0	399.6
	Control Z6-45	152.4	194.5	3.52	43.8	427.5	63.33	0	399.6
Cao et al. [35]	A-C A-2 A-3	150	222.5	2.70	30.5	1472.6	981.7	56.54	361
	L-C L-2 L3	150	222.5	2.92	30	1472.6	981.7	56.54	361
Miyuchi et al. [36]	A- Control AN-1/5Z-3 AN-1/2Z-3	125	165	3.03	35.1	981.74	0	0	362
Uji [37]	Control 5 6 7 3	100	167	2.55	24.12	402.12	402.12	0	382.5
Monti and Liotta [21]	Control SF90 UF90 US60	250	402	3.48	10.64	1256.6	628.31	100.5	500
Taerwa et al. [38]	Control BS-4 BS-5 BS-6 BS-7	200	402	3.11	36.2	1884.95	1941.5	56.54	559
Umezu et al. [39]	Control AS1 AS2 AS3 CS3	150	272	2.94	43	422	0	0	1720
	Control CS1 CS2	300	257	2.95	40.5	844	0	0	1720
	Control AB1 AB2 AB34	150 300	253	3	40	830 1660	0	0	1070

Table 3-1 (Contd.)

		b_w (mm)	d (mm)	a/d	f_c (MPa)	A_{sb} (mm)^2	A_{st} (mm)^2	A_s (mm)^2	f_y (MPa)
Umezu et al. [39]	AB5 AB6 AB7 AB8	300 600	253	3	40	1660 3320	0	0	1070
	AB9 AB10 AB11	450 550	399 499	3 3	40 40	4020 5628	0	0	1040
Adhikary and Mutsuyoshi [40]	Control B-4 B-7 B-8	150	170	3	31.5 34.4 35.4	760.265	0	0	582
Funakawa et al. [41]	Control S2 S3 S4	600	510	2.5	30	11256	11256	156	1038
Park et al. [42]	Control 2 3	100	185	2.75	25.4	396	0	0	500
Li et al. [43]	Control BO1 BO2 BO3	130	280	2.75	38	402	100.53	0	550
Sato et al. [44]	Control S2 S3 S4 S5	200	260	2.7	37.6 45.2 41.3 37.5 39.7	1701.2	0	0	371
Beber [45]	Control V9 V10,11 V12,18,20 V12,14 V19 V13 V15,16 V16,18 V22,20 V21,22	150	250	2.96	32.8	1206.37	402.1	0	625.2

Table 3-2: FRP retrofit details

		FRP achorage	t_{frp} (mm)	w_{frp} (mm)	s_{frp} (mm)	ρ_{frp}	E_{frp} (MPa)	$f_{frp,u}$ (MPa)
Triantafillou [18]	S1	strip	0.155	30	60	0.0022	230000	3300
	S1-45	strip-45^0		30		0.0022		
	S2	strip		45		0.0033		
	S2-45	strip-45^0		45		0.0033		
	S3	sheet		60		0.0044		
	S3-45	sheet-45^0		60		0.0044		
Al Sulaimani [24]	SO	strip	3	20	50	0.016	16000	200
	WO	sheet		50		0.04		
	JO	U-cont		50		0.04		
Zhang and Teng [34]	Z6-90	strip	1.5	40	127	0.0062	165000	2800
	Z6-45	strip			179.6	0.00438		
Cao et al. [35]	A-2	strip	0.167	30	100	0.000668	249000	3635
	A-3	strip			150	0.000445		
	L-2	strip	1.2	25	50	0.008	5300	112
	L3	strip			100	0.004		
Miyuchi et al. [36]	AN-1/5Z-3	strip	0.11	20	100	0.00352	230000	3480
	AN-1/2Z-3	strip		500		0.00088		
Uji [37]	5	sheet	0.097	1	1	0.00194	230456	2647
	6	sheet-45^0	0.097			0.00194		
	7	2-sheets	0.194			0.00388		
	3	wrap	0.097			0.00194		
Monti and Liotta [21]	SF90	sheet	0.22	1	1	0.00117	390000	3120
	UF90	U-sheet		1	1	0.001173		
	US60	U-strip		150	346.41	0.00051		
Taerwa et al. [38]	BS-4	U-sheet	0.11	1	1	0.0011	279520	3494
	BS-5	U-strip		50	400	0.000138		
	BS-6	U-strip		50	600	9.2E-05		
	BS-7	wrap-strip		50	200	0.0028		
Umezu et al. [39]	AS1	wrap-sheet	0.044	1	1	0.0005866	7300	2700
	AS2	wrap-strip		100	200	0.000293		
	AS3	wrap-sheet	0.088	1	1	0.0011732	244000	
	CS3	wrap-strip				0.00074		
	CS1	wrap-sheet	0.111	100	200	0.00037		
	CS2	wrap-strip				0.000471		
	AB1	wrap-sheet	0.044	1	1	0.000587	73000	
	AB2	wrap-sheet				0.000293		
	AB34	wrap-sheet	0.088			0.000587		
	AB5	wrap-sheet	0.144			0.000587		

Table 3-2 (Contd.)

		FRP achorage	t_{frp} (mm)	w_{frp} (mm)	s_{frp} (mm)	ρ_{frp}	E_{frp} (MPa)	$f_{frp,u}$ (MPa)
Umezu et al. [39]	AB6	wrap-sheet	0.216	1	1	0.00144	73000	2700
	AB7	wrap-sheet	0.288			0.00192		
	AB8	wrap-sheet	0.144			0.00048		
	AB9	wrap-sheet				0.00064		
	AB10	wrap-sheet				0.000524		
	AB11	wrap-sheet	0.288			0.001047		
Adhikary and Mutsuyoshi [40]	B-4	sheet	0.167	1	1	0.00167	23000	3400
	B-7	U-sheet				0.00167		
	B-8	U-sheet				0.002226		
Funakawa et al. [41]	S2	wrap-sheet	0.167	1	1	0.000556	240000	3800
	S3	wrap-sheet	0.334			0.001113		
	S4	wrap-sheet	0.501			0.00167		
Park et al. [42]	2	sheet	0.16	1	1	0.0032	240000	3400
	3	strip	1.2	25	75	0.008	155000	2400
Li et al. [43]	B01	sheet	1.5	1	1	0.01153	15000	209
	B02	sheet				0.0173		
	B03	sheet				0.02154		
Sato et al. [44]	S2	strip	0.111	30	60	0.00055	230000	3480
	S3	u-strip						
	S4	sheet		1	1	0.0011		
	S5	u-sheet						
Beber [45]	V9	strip	0.11	50	141.4	0.0005233	230000	3400
	V10,11	U-strip						
	V12,18,20	wrap-strip						
	V12,14	side-strip						
	V19	U-strip						
	V13	sheet		1	1	0.00146		
	V15,16	U-sheet						
	V16,18	wrap-sheet						
	V22,20	strip	1.4	50	100	0.00933	205000	2500
	V21,22	sheet			141.4	0.0066		

Table 3-3: FRP shear strength contribution of RC beams with a/d >2.5

Experimental		ACI Model			Triantafillou Model			Cheng-Teng Model			Monti-Liotta Model			Proposed Model		
	V_{frp} (kN)	V_{frp} (kN)	ε_{theo}	R_{theo}	V_{frp} (kN)	ε_{theo}	R_{theo}	V_{frp} (kN)	ε_{theo}	R_{theo}	V_{frp} (kN)	ε_{theo}	R_{theo}	V_{frp} (kN)	ε_{theo}	R_{theo}
Triantafillou [18]																
S1	12.4	NA	NA	NA	10.91	-12.05	0.88	11.06	-10.80	0.89	5.39	-56.51	0.43	9.70	-21.77	0.78
S1-45	14.05	NA	NA	NA	15.42	9.77	1.10	14.70	4.61	1.05	7.06	-49.76	0.50	10.90	-22.42	0.78
S2	14.37	NA	NA	NA	13.04	-9.32	0.91	12.67	-11.83	0.88	5.76	-59.94	0.40	11.90	-17.22	0.83
S2-45	15.45	NA	NA	NA	18.43	19.32	1.19	16.09	4.16	1.04	8.48	-45.14	0.55	18.70	21.04	1.21
S3	11.87	NA	NA	NA	14.79	24.59	1.25	13.16	10.83	1.11	3.41	-71.32	0.29	11.90	0.21	1.00
S3-45	12.15	NA	NA	NA	20.92	72.20	1.72	15.02	23.59	1.24	6.94	-42.92	0.57	17.80	46.50	1.47
Al Sulaimani [24]																
SO	8	4.20	-47.51	0.52	21.11	163.85	2.64	9.20	15.06	1.15	5.70	-28.70	0.71	8.30	3.75	1.165
Cao et al. [35]																
A-2	22	13.86	-37.00	0.63	31.76	44.39	1.44	43.86	99.37	1.99	30.16	37.09	1.37	34.20	55.45	1.55
A-3	23	9.23	-59.85	0.40	26.57	15.50	1.16	32.02	39.20	1.39	20.90	-9.13	0.91	23.70	3.04	1.03
L-2	20	NA	NA	NA	14.24	-28.81	0.71	20.62	3.11	1.03	17.97	-10.16	0.90	16.90	-15.50	0.85
L3	17.5	NA	NA	NA	10.50	-40.03	0.60	14.49	-17.17	0.83	10.69	-38.92	0.61	10.40	-40.57	0.59
Miyauchi et al. [36]																
AN-1/5Z-3	18.75	2.30	-87.76	0.12	15.07	-19.63	0.80	27.58	47.07	1.47	18.08	-3.60	0.96	21.50	14.67	1.15
Monti and Liotta [21]																
SF90	17.5	55.97	219.84	3.20	100.77	475.82	5.76	33.79	93.07	1.93	20.66	18.05	1.18	20.00	14.29	1.14
UF90	30	36.39	127.41	2.27	87.06	444.15	5.44	41.59	159.91	2.60	39.87	149.16	2.49	30.83	92.70	1.93
US60	16	61.11	103.69	2.04	100.77	235.90	3.36	51.80	72.66	1.73	47.94	59.82	1.60	39.43	31.44	1.31
Taerwa et al. [38]																
BS-4	115.4	101.81	-11.77	0.88	105.04	-8.98	0.91	149.48	29.53	1.30	182.76	58.37	1.58	182.10	57.80	1.58
BS-5	33.4	12.73	-61.90	0.38	31.64	-5.26	0.95	39.17	17.26	1.17	49.83	49.20	1.49	45.10	35.03	1.35
BS-6	30.1	8.48	-71.83	0.28	23.81	-20.89	0.79	26.47	-12.07	0.88	33.86	12.48	1.12	30.00	-0.33	1.00
BS-7	98.9	21.71	-78.05	0.22	51.40	-48.02	0.52	74.46	-24.71	0.75	96.96	-1.96	0.98	46.00	-53.49	0.47
Umezu et al. [39]																
AS1	27.50	6.99	-74.59	0.25	39.88	45.03	1.45	59.24	115.41	2.15	74.02	169.15	2.69	35.54	29.25	1.29
AS2	26.00	3.49	-86.57	0.13	27.61	6.18	1.06	35.19	35.36	1.35	43.68	67.98	1.68	21.12	-18.78	0.81
AS3	50.30	13.98	-72.21	0.28	57.59	14.49	1.14	99.64	98.09	1.98	126.42	151.32	2.51	59.79	18.86	1.19
CS1	86.60	55.68	-35.70	0.64	130.88	51.13	1.51	214.73	147.96	2.48	183.18	111.52	2.12	81.27	-6.15	0.94
CS2	31.60	27.84	-11.89	0.88	80.57	154.97	2.55	127.67	304.01	4.04	106.92	238.34	3.38	48.32	52.92	1.53

Table 3-3 (Contd.)

Experimental		ACI Model			Triantafillou Model			Cheng-Teng Model			Monti-Liotta Model			Proposed Model		
	V_{frp} (kN)	V_{frp} (kN)	ε_{theo}	R_{theo}	V_{frp} (kN)	ε_{theo}	R_{theo}	V_{frp} (kN)	ε_{theo}	R_{theo}	V_{frp} (kN)	ε_{theo}	R_{theo}	V_{frp} (kN)	ε_{theo}	R_{theo}
CS3	52.30	18.76	-64.14	0.36	51.51	-1.50	0.98	79.65	52.29	1.52	66.23	26.63	1.27	30.15	-42.36	0.58
AB1	63.50	6.50	-89.76	0.10	36.19	-43.00	0.57	66.54	4.79	1.05	83.48	31.47	1.31	39.92	-37.13	0.63
AB2	45.60	6.49	-85.76	0.14	50.09	9.84	1.10	79.02	73.30	1.73	99.23	117.60	2.18	47.41	3.98	1.04
AB34	89.10	13.01	-85.40	0.15	72.39	-18.76	0.81	133.08	49.36	1.49	169.98	90.77	1.91	79.85	-10.38	0.90
AB5	126.60	13.01	-89.72	0.10	72.39	-42.82	0.57	133.08	5.12	1.05	172.85	36.53	1.37	79.85	-36.93	0.63
AB6	119.60	31.91	-73.32	0.27	116.47	-2.61	0.97	260.92	118.16	2.18	343.95	187.59	2.88	156.55	30.90	1.31
AB7	112.60	42.55	-62.21	0.38	135.66	20.48	1.20	323.79	187.56	2.88	432.43	284.04	3.84	194.27	72.53	1.73
AB8	240.00	21.28	-91.13	0.09	130.13	-45.78	0.54	228.87	-4.64	0.95	297.38	23.91	1.24	137.32	-42.78	0.57
AB9	163.00	33.55	-79.41	0.21	179.27	9.98	1.10	337.77	107.22	2.07	427.53	162.29	2.62	202.66	24.33	1.24
AB10	294.00	41.99	-85.72	0.14	246.47	-16.17	0.84	434.84	47.90	1.48	545.33	85.49	1.85	260.90	-11.26	0.89
AB11	347.00	83.91	-75.82	0.24	355.70	2.51	1.03	730.88	110.63	2.11	931.74	168.51	2.69	438.53	26.38	1.26
Adhikary and Mutsuyoshi [40]																
B-4	19.40	18.59	-4.17	0.96	35.50	82.99	1.83	21.45	10.56	1.11	19.61	1.09	1.01	29.30	51.03	1.51
B-7	29.30	19.71	-32.71	0.67	36.69	25.21	1.25	34.72	18.49	1.18	71.65	144.52	2.45	60.77	107.41	2.07
B-8	46.60	26.79	-42.52	0.57	42.08	-9.70	0.90	72.98	56.62	1.57	91.63	96.64	1.97	91.63	96.63	1.97
Funakawa et al. [41]																
S2	242.00	163.33	-32.51	0.67	356.61	47.36	1.47	711.06	193.82	2.94	910.57	276.27	3.76	426.63	76.29	1.76
S3	346.00	326.95	-5.50	0.94	579.68	67.54	1.68	1335.92	286.10	3.86	1755.34	407.32	5.07	801.55	131.66	2.32
S4	493.00	490.58	-0.49	1.00	770.09	56.21	1.56	1905.77	286.57	3.87	2552.92	417.83	5.18	1143.46	131.94	2.32
Park et al. [42]																
3	18.10	29.50	62.97	1.63	39.80	119.89	2.20	23.06	27.40	1.27	7.96	-56.02	0.44	18.15	0.28	1.00
Sato et al. [44]																
S2	68.40	25.33	-62.97	0.37	50.82	-25.71	0.74	91.59	33.90	1.34	79.34	15.99	1.16	90.30	32.02	1.32
S4	64.20	45.13	-29.70	0.70	64.29	0.15	1.00	103.49	61.20	1.61	66.81	4.06	1.04	81.20	26.48	1.26
Li et al. [43]																
BO1	16.00	32.88	105.53	2.06	54.04	237.77	3.38	8.03	-49.79	0.50	21.92	37.02	1.37	21.40	33.75	1.34
BO2	31.33	49.34	57.47	1.57	64.68	106.43	2.06	23.59	-24.72	0.75	31.62	0.91	1.01	32.70	4.36	1.04
BO3	29.33	61.43	109.44	2.09	71.23	142.83	2.43	42.45	44.71	1.45	38.61	31.62	1.32	41.40	41.14	1.41
Beber [45]																
V9	48.95	19.06	-61.06	0.39	37.05	-24.31	0.76	78.65	60.69	1.61	63.65	30.05	1.30	69.42	41.83	1.42
V10,11	48.48	19.06	-60.69	0.39	37.05	-23.59	0.76	89.46	84.54	1.85	118.71	144.87	2.45	118.71	144.86	2.45

Table 3-3 (Contd.)

Experimental		ACI Model			Triantafillou Model			Cheng-Teng Model			Monti-Liotta Model			Proposed Model		
	V_{frp} (kN)	V_{frp} (kN)	ε_{theo}	R_{theo}	V_{frp} (kN)	ε_{theo}	R_{theo}	V_{frp} (kN)	ε_{theo}	R_{theo}	V_{frp} (kN)	ε_{theo}	R_{theo}	V_{frp} (kN)	ε_{theo}	R_{theo}
V12,18,20	71.00	25.53	-64.04	0.36	49.41	-30.41	0.70	115.89	63.22	1.63	153.95	116.83	2.17	69.53	-2.07	0.98
V12,14	39.73	19.06	-52.03	0.48	44.98	13.22	1.13	61.90	55.81	1.56	41.97	5.64	1.06	34.07	-14.25	0.86
V19	59.85	19.06	-68.16	0.32	44.98	-24.84	0.75	67.47	12.74	1.13	92.03	53.76	1.54	91.44	52.78	1.53
V13	66.96	37.60	-43.84	0.56	49.96	-25.39	0.75	92.60	38.30	1.38	62.35	-6.88	0.93	70.45	5.22	1.05
V15,16	68.48	37.60	-45.09	0.55	49.96	-27.04	0.73	105.33	53.82	1.54	121.12	76.89	1.77	121.12	76.88	1.77
V16,18	136.57	50.37	-63.12	0.37	79.51	-41.78	0.58	192.96	41.29	1.41	262.67	92.34	1.92	115.57	-15.37	0.85
V22,20	70.79	95.30	34.63	1.35	107.41	51.73	1.52	66.97	-5.40	0.95	24.00	-66.09	0.34	56.70	-19.90	0.80
V21,22	73.72	95.34	29.33	1.29	130.44	76.93	1.77	79.92	8.41	1.08	30.67	-58.39	0.42	58.40	-20.78	0.79
All (57)	Average		-29.33	0.71		39.51	1.40		58.84	1.59		64.66	1.65		21.76	1.22
	St. dev.		68.14	0.68		103.77	1.04		76.03	0.76		108.44	1.08		46.13	0.46
	Min		-91.13	0.09		-48.02	0.52		-49.79	0.50		-71.32	0.29		-53.49	0.47
	Max		219.84	3.20		475.82	5.76		304.01	4.04		417.83	5.18		144.86	2.45
Side bonding (25)	Average		15.28	1.15		56.34	1.56		22.25	1.22		-15.25	0.85		9.27	1.09
	St. dev.		84.84	0.85		113.14	1.13		36.34	0.36		35.07	0.35		27.36	0.27
	Min		-87.76	0.12		-40.03	0.60		-49.79	0.50		-71.32	0.29		-40.57	0.59
	Max		219.84	3.20		475.82	5.76		99.37	1.99		37.09	1.37		55.45	1.55
U-jacketing (10)	Average		-16.36	0.84		58.49	1.58		49.35	1.49		84.57	1.85		69.52	1.70
	St. dev.		72.02	0.72		157.01	1.57		48.95	0.49		47.50	0.47		42.66	0.43
	Min		-71.83	0.28		-27.04	0.73		-12.07	0.88		12.48	1.12		-0.33	1.00
	Max		127.41	2.27		444.15	5.44		159.91	2.60		149.16	2.49		144.86	2.45
Wrapping (22)	Average		-63.96	0.36		8.86	1.09		104.49	2.04		148.26	2.48		14.65	1.15
	St. dev.		28.27	0.28		48.38	0.48		95.60	0.96		116.37	1.16		52.31	0.52
	Min		-91.13	0.09		-48.02	0.52		-24.71	0.75		-1.96	0.98		-53.49	0.47
	Max		-0.49	1.00		154.97	2.55		304.01	4.04		417.83	5.18		131.94	2.32

4. FINITE ELEMENT MODELING

4.1 Finite element formulation

This study adopts a two-node frame FE based on a force-based formulation [46]-[48] with Euler-Bernoulli kinematic assumptions and linear geometry (i.e., small deformations and small displacements) to model the behavior of the RC beams retrofitted with FRP in shear. Force-based frame elements are gaining wide recognition over the traditional displacement-based frame elements owing to their ability to achieve converged response (within a given level of accuracy) with significantly smaller number of elements at a small additional computational cost per element. The displacement-based formulation uses cubic and linear Hermitian polynomials to approximate the transverse displacement field and linear lagrangian shape functions for the axial displacement fields. By contrast the force-based formulation uses interpolation functions for the internal forces, which satisfy the equilibrium of axial forces and bending moments at any point along the element [46][48].

The challenge faced in case of force-based frame elements was their implementation in general-purpose FE programs, which in general use direct stiffness assembly approach that is consistent with displacement-based formulations at the element level. Spacone et al. [46][48] proposed a frame element to overcome this challenge by using a state determination procedure that iteratively determines the element resisting forces and stiffness matrix [48], based on the Newton-Raphson iteration scheme. In this study, the non-iterative state determination scheme proposes by Neuenhofer and Filippou [48] is employed. The Gauss-Lobatto integration scheme is used in the element state determination, in which the number of integration points (i.e., monitored cross sections) is defined by the user. In addition, a two dimensional fiber discretization of the frame cross section is used to model nonlinear behavior of the corresponding

cross section, as shown in Figure 4-1 for a two dimensional problem in which the fibers reduce to layers.

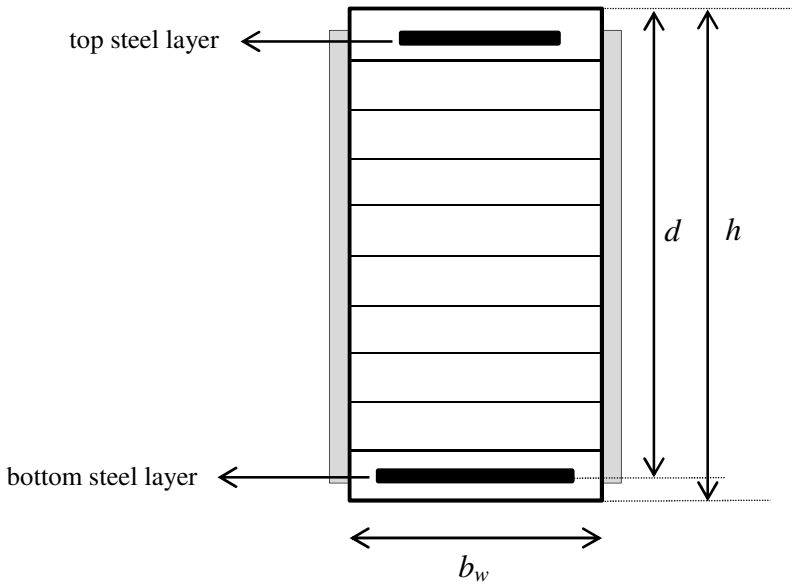

Figure 4-1: Fiber layer discretization of frame cross section

4.2 Computation of cross-sectional bending moment and axial force

The bending moment and axial force at any monitored cross section are computed using a fiber discretization. The stress-strain behavior of each layer within the cross section is defined by a realistic one-dimensional nonlinear constitutive model. The constitutive models adopted for concrete and steel are the Kent-Scott-Park model [50] and the bilinear hysteric model with kinematic hardening, respectively. The uniaxial Kent-Scott-Park concrete model assumes that the tensile strength of concrete is negligible and incorporates the degradation of strength and stiffness after the concrete material reaches the peak strength. The bilinear steel model assumes a linear elastic behavior up to the yield point, beyond which the stiffness is defined by the strain hardening modulus. A typical cyclic response of the adopted concrete and steel models is shown

in Figure 4-2 and Figure 4-3, respectively. The contribution to the bending and axial force due to the FRP material used for shear retrofit is neglected.

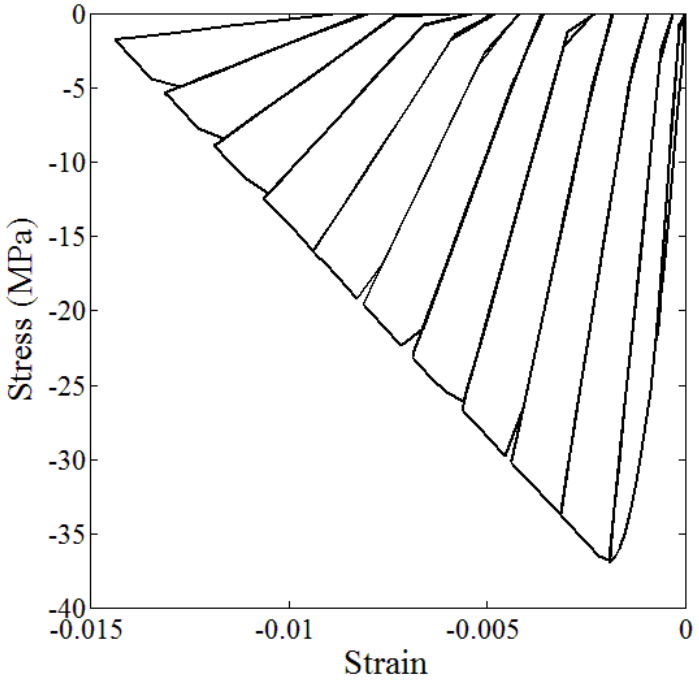

Figure 4-2: Kent-Scott-Park concrete model: Cyclic-stress strain response

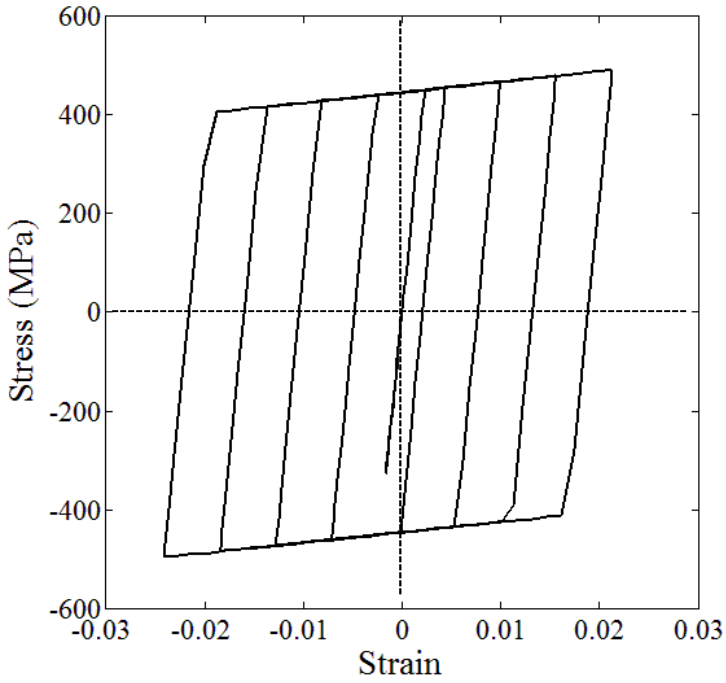

Figure 4-3: Bilinear steel model: Cyclic stress-strain response

4.3 Evaluation of shear strength of a cross section

The shear strength contributions of concrete and steel for all the RC beams retrofitted with FRP considered in this study are computed from the shear strength of the corresponding control beams (i.e., without FRP retrofit). The strength contribution of the FRP is computed according to the newly proposed model (see Chapter 3).

Furthermore, this study takes into consideration the reduction in the shear strength of RC beams due to reduction in the shear strength of concrete. According to Priestley [51], the reduction in the concrete strength is due to formation of plastic hinges in an element, which causes widening of shear cracks, thereby resulting in reduction of shear transfer by aggregate interlock. Three different conditions can be recognized: (a) if the flexural strength is lower than the residual shear strength, the beam undergoes a ductile flexural failure; (b) if the flexural strength is higher than the initial shear strength, the beam undergoes a brittle shear failure, (c) if the flexural strength is between the initial and residual shear strength, the beam fails in shear with yielding (mixed flexure-shear failure) [50].

Priestley et al. [51] proposed the following relationship between the residual shear strength of concrete, V_r, and the curvature ductility at the section (see Figure 4-4),

$$V_r = k \cdot V_c \tag{4.1}$$

where k is the reduction factor given by

$$k = \begin{cases} 1 & \text{for } \mu_x \le 3 \\ 1.5625 - 0.1875 \cdot \mu_x & \text{for } 3 < \mu_x < 7 \\ 0.25 & \text{for } \mu_x \ge 7 \end{cases} \tag{4.2}$$

in which $\mu_x = \frac{\chi_{max}}{\chi_y}$ is the maximum curvature ductility, χ_{max} is maximum curvature reached at peak strength, and χ_y is the curvature at which yielding of the rebars occurs.

Therefore, the relation adopted in this study to evaluate the shear strength, V_t at a given cross-section of a frame element is

$$V_t = \min\left(V_{R,max}, V_r + V_s + V_{frp}\right) \tag{4.3}$$

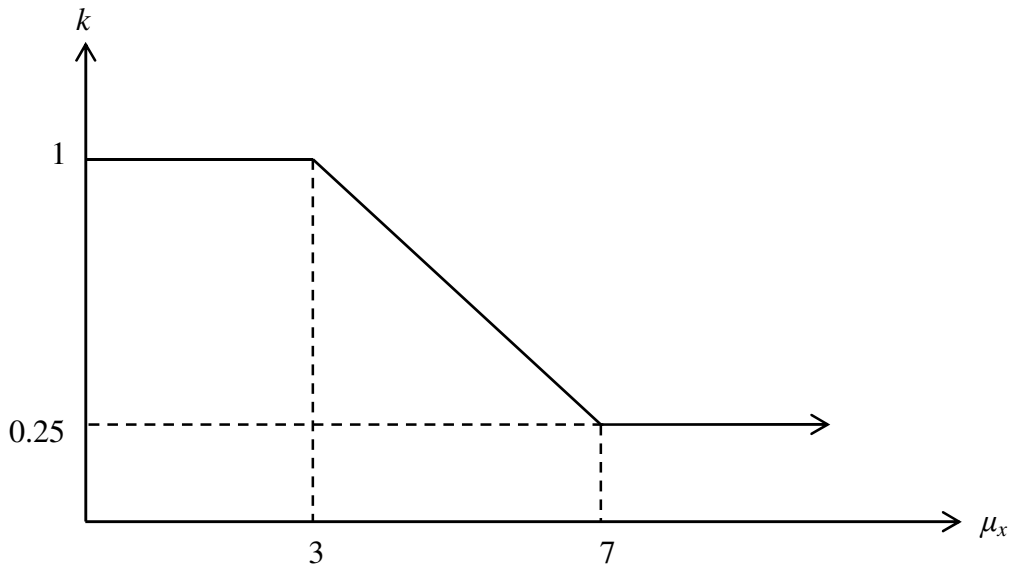

Figure 4-4: Priestley's rule for shear strength reduction

4.4 Computer implementation and numerical simulation

The nonlinear FE analysis results presented in this study for RC beams retrofitted with FRP in shear retrofit were performed using FEDEASLab [52], which is a Matlab toolbox [53] suitable for linear and nonlinear structural analysis. The element and section libraries were extended to predict the response of RC beams with FRP shear retrofit. The nonlinear FE analysis was performed to simulate the response of the FRP shear retrofitted RC beams, tested experimentally by several researchers [18]-[21],[33]-[45] (see Section 3.7). The RC beams considered in this

study were all tested as simply supported beams subjected to three- or four-point loading. The experimental results of these beams were mostly presented in terms of ultimate load carrying capacity. Thus, in order to numerically predict the load carrying capacity of the RC beams, the two FE models described in Figure 4-5 and Figure 4-6 were employed for 3-point and 4-point bending tests. Five Gauss-Lobatto integration points were used for each element of the FE model. A displacement controlled loading technique, based on the Newton-Raphson iterative procedure was adopted. Vertical displacements were applied at the loading points and the corresponding internal resisting forces were computed [54]. Only one half of the beam was modeled, thus taking the advantage of symmetry of the beams.

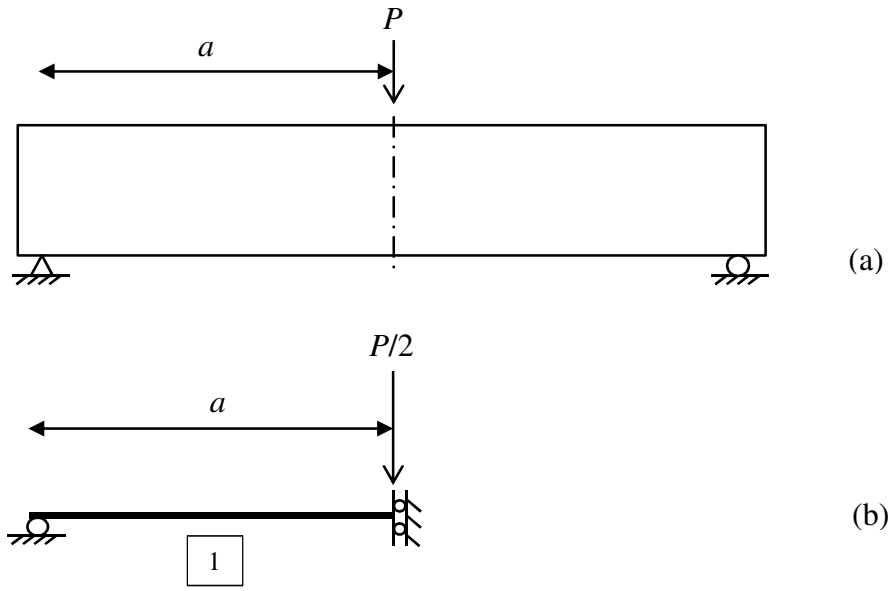

Figure 4-5: Three-point bending test: (a) Experimental set up, and (b) FE mesh

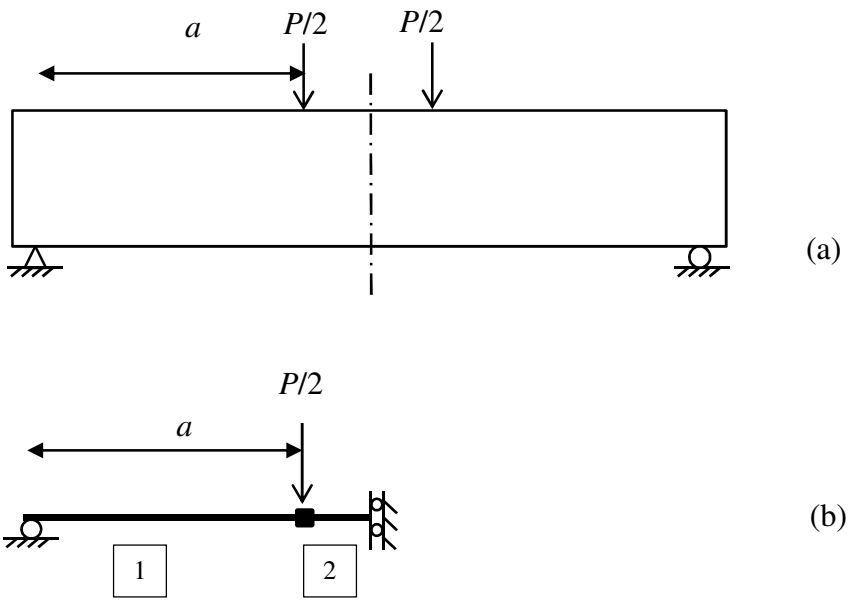

Figure 4-6: Four-point bending test: (a) Experimental set up, and (b) FE mesh

4.5 Comparison of numerical and experimental results

The efficiency of the developed frame FE was evaluated by comparing the numerically computed, $V_{t,num}$, and experimentally determined, V_{exp}, shear strength of the considered RC beams. The ratio of numerical to experimental shear strength, R_{FE}, was also computed for all the considered FRP shear retrofitted RC beams as

$$R_{FE} = \frac{V_{t,num}}{V_{exp}} \tag{4.3}$$

The experimental database consists of 69 FRP shear retrofitted RC beams with $a/d \geq 2.5$. The cross-sectional and material properties of all the RC beams considered in this study, as well as the FRP retrofit details, are summarized in Table 3-1 and Table 3-2, respectively. Table 4-1 shows the comparison of the numerical and experimental load carrying capacity of the considered RC beams and the failure mode observed experimentally and predicted by the FE analysis.

It is observed that the numerical simulations of the response of the FE models are in good agreement with the corresponding experimentally measured shear strength and the observed failure modes. Considering all beams, the mean value of the ratio R_{FE} is 1.09, and the standard deviation is 0.21. For beams failing only in pure shear, the mean value of the ratio R_{FE} is 1.11 and the standard deviation is 0.22. For beams failing only in mixed flexure-shear, the mean value of the ratio R_{FE} is 1.04 and the standard deviation is 0.13. For beams failing only in flexure, the mean value of the ratio R_{FE} is 0.92 and the standard deviation is 0.09. It is observed that the mean and standard deviation of R_{FE} are relatively low when compared to other studies on shear strength of RC beams available in the literature [56]. This phenomenon is due to the fact that the FE analysis performed in this study considers only the variability of the shear strength due to FRP retrofit and to the reduction of the shear strength contribution of the concrete. In fact, in computing the shear strength of the beams using Equation (4.3), the variability connected with the contributions V_c and V_s is minimized by employing the experimental values reported in the referenced literature. Therefore, the bias and the variability introduced by numerical estimation of V_c and V_s were practically eliminated. This result also suggests that the variability of the concrete and steel contributions to the total shear strength of RC beams retrofitted in FRP can be larger than the variability of the FRP contribution.

Figure 4-7 graphically reproduces the results of the shear strength provided in Table 4-1. The experimental and numerical shear strengths are represented on horizontal and vertical axes respectively. The dashed line in the Figure 4-7 represents the perfect agreement between the computed and experimental results, i.e., $R_{FE} = 1$.

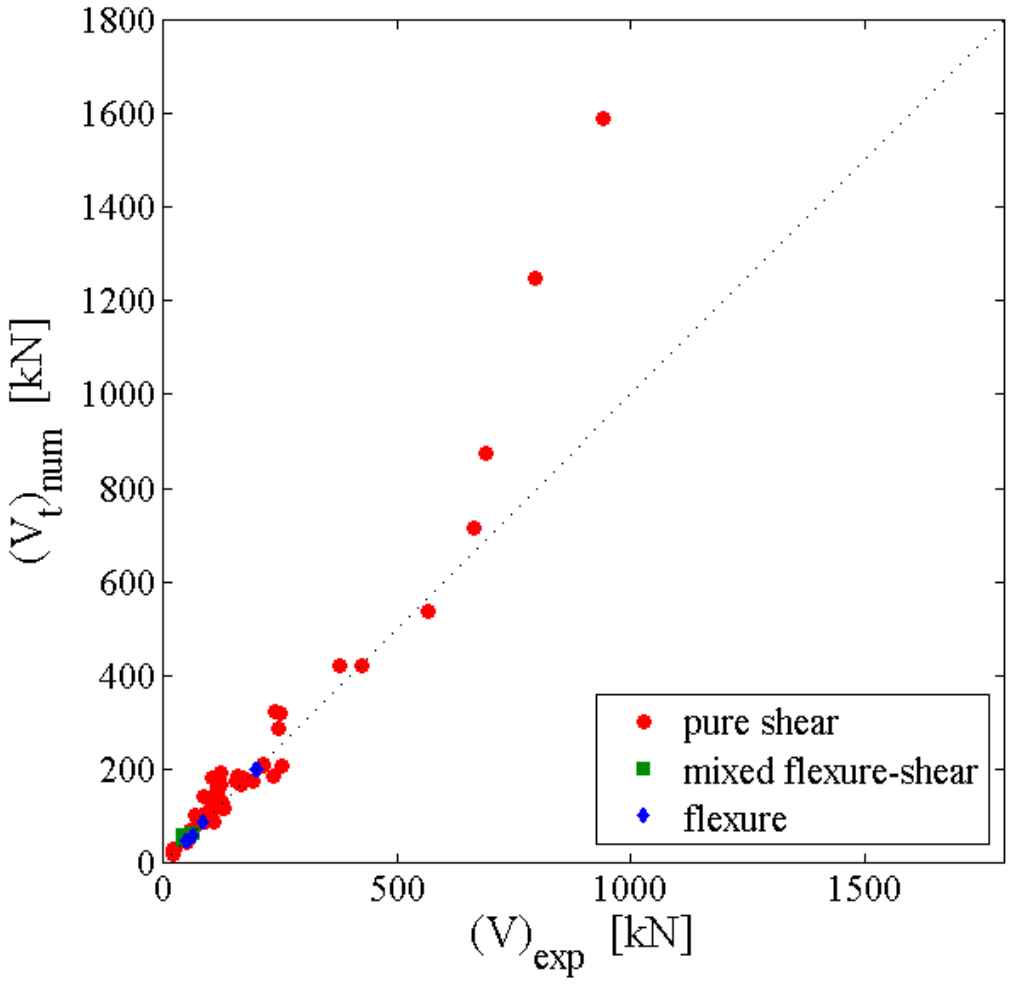

Figure 4-7: Comparison of numerical and experimental shear strengths

Furthermore, it is observed that the proposed FE model is able to predict the different failure modes with excellent agreement with the experimental response. The experimentally observed and numerically identified failure modes are in disagreement only for one beam among all beams considered (i.e., beam AN-1/2Z-3 in [36]). The failure modes predicted by the FE model are: (a) pure shear, (b) mixed flexure-shear, and (c) flexure (see Figure 4-8). In experimental tests, RC beams can fail in shear by a combination of one or more failure modes, e.g., FRP rupture, FRP debonding/delamination/peeling, diagonal tension (see Section 2.1 and Section 2.3). The pure shear and mixed flexure-shear failure modes identified by the FE analysis refer to a single or a

combination of physically/experimentally observed failure modes (e.g., diagonal tension, shear debonding, shear cracking, strip delamination, peeling) as indicated in Table 4-1, where the failure modes identified by the authors of the experimental tests are reported together with the failure modes identified using FE analysis.

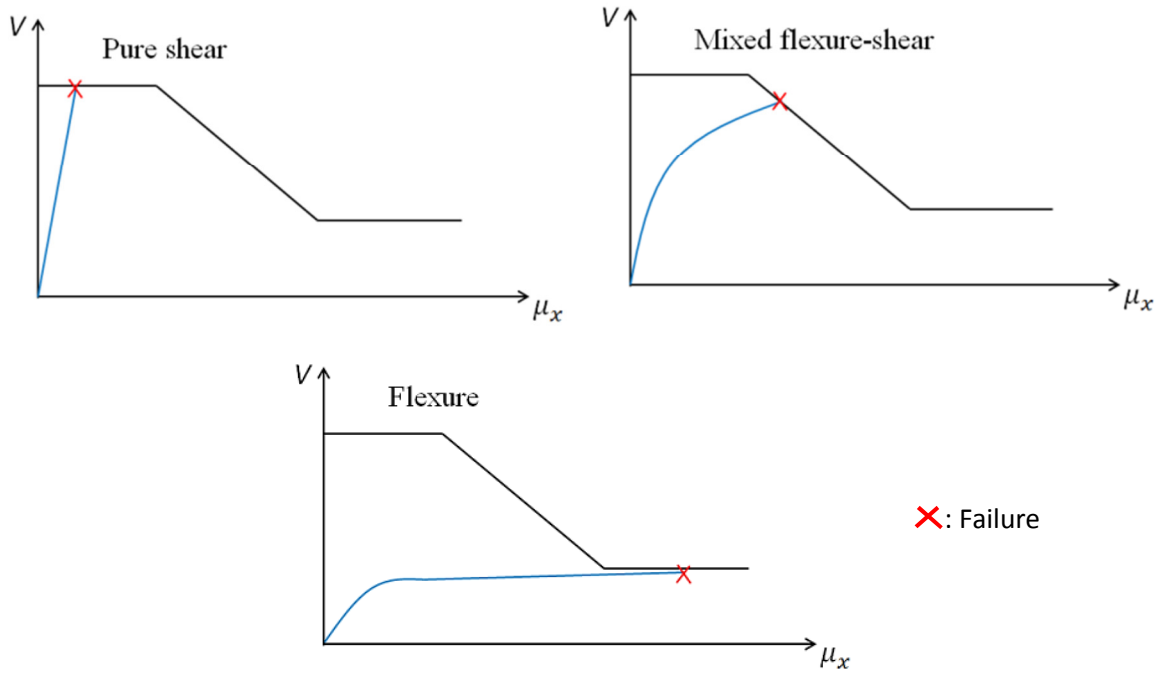

Figure 4-8: Graphical representation of the different failure modes identified by FE analysis

Among the 69 RC beams considered, 57 beams failed in pure shear, six beams failed in mixed flexure-shear, and six beams failed in flexure. The mixed flexure-shear failure mode captures the reduction of shear strength given by Priestley [50]. Figure 4-9 shows the shear strength and the shear-curvature relation obtained from FE analysis at the section with highest moment for the beam identified as "WO" in [24].

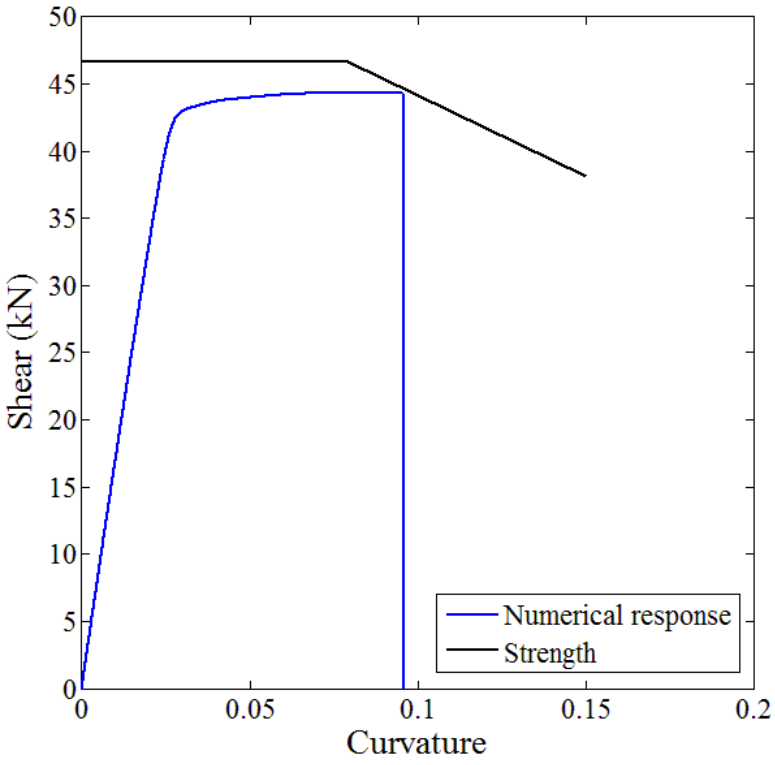

Figure 4-9: Mixed failure mode in RC beam identified as “WO” in [24]

Table 4-1: Comparison of numerical and experimental shear strengths

		V_{exp} [kN]	$V_{t,num}$ [kN]	R_{FE}	Failure mode	
					Experimental	Numerical
Triantafillou [18]	S1	20.60	17.90	0.87	shear debonding	pure shear
	S1-45	22.25	19.10	0.86	shear debonding	pure shear
	S2	22.58	20.14	0.89	shear debonding	pure shear
	S2-45	23.65	26.88	1.14	shear debonding	pure shear
	S3	20.08	20.14	1.00	shear debonding	pure shear
	S3-45	20.35	26.00	1.28	shear debonding	pure shear
Al Sulaimani [24]	SO	41.35	47.50	1.15	diagonal tension	pure shear
	WO	43.60	44.42	1.02	diagonal tension	mixed shear-flexure
	JO	50.10	46.60	0.93	flexure	flexure
Zhang and Teng [34]	Z6-90	63.86	60.50	0.95	strip delamination	mixed shear-flexure
	Z6-45	55.63	44.50	0.80	flexural cracking	flexure
Cao et al. [35]	A-2	92.50	104.70	1.13	shear cracking	pure shear
	A-3	93.50	94.20	1.01	shear cracking	pure shear
	L-2	52.00	48.90	0.94	shear cracking	pure shear
	L3	49.50	42.40	0.86	shear cracking	pure shear
Miyuachi et al. [36]	AN-1/5Z-3	75.20	82.20	1.09	diagonal tension	pure shear
	AN-1/2Z-3 *	85.95	85.80	0.99	diagonal tension	flexure
Uji [37]	5	45.34	54.30	1.19	shear	mixed shear-flexure
	6	57.79	54.10	0.94	shear	mixed shear-flexure
	7	45.34	54.60	1.2	shear	mixed shear-flexure
	3	59.29	54.10	0.91	shear	mixed shear-flexure
Monti and Liotta [21]	SF90	112.50	115.00	1.02	shear	pure shear
	US60	111.00	141.83	1.28	shear	pure shear
	UF90	125.00	164.43	1.32	shear	pure shear
Taerwa et al. [38]	BS-4	252.00	318.60	1.26	diagonal tension	pure shear
	BS-5	170.00	181.60	1.07	peeling	pure shear

Table 4-1 (Contd.)

		V_{exp} [kN]	$V_{t,num}$ [kN]	R_{FE}	Failure mode	
					Experimental	Numerical
Taerwa et al. [38]	BS-6	166.70	166.50	0.99	peeling	pure shear
	BS-7	235.50	182.50	0.77	diagonal tension	pure shear
Umezu et al. [39]	AS1	91.20	99.24	1.09	shear	pure shear
	AS2	89.70	84.82	0.95	shear	pure shear
	AS3	114.00	123.49	1.08	shear	pure shear
	CS1	214.00	208.28	0.97	Shear	pure shear
	CS2	159.00	175.72	1.11	shear	pure shear
	CS3	116.00	93.85	0.81	shear	pure shear
	AB1	110.00	86.42	0.77	shear	pure shear
	AB2	173.00	174.81	1.01	shear	pure shear
	AB34	216.00	207.25	0.96	shear	pure shear
	AB5	254.00	207.25	0.82	shear	pure shear
	AB6	247.00	283.95	1.15	shear	pure shear
	AB7	240.00	321.67	1.34	shear	pure shear
	AB8	424.00	421.32	0.99	shear	pure shear
	AB9	379.00	418.66	1.11	shear	pure shear
	AB10	569.00	535.90	0.94	shear	pure shear
	AB11	667.00	713.53	1.07	shear	pure shear
Adhikary and Mutsuyoshi [40]	B-4	58.60	68.30	1.17	shear debonding	pure shear
	B-7	68.50	99.70	1.46	shear debonding	pure shear
	B-8	85.80	141.00	1.64	shear debonding	pure shear
Funakawa et al. [41]	S2	691.00	875.63	1.27	shear	pure shear
	S3	795.00	1250.55	1.57	shear	pure shear
	S4	942.00	1592.46	1.69	shear	pure shear
Park et al. [42]	2	65.20	55.00	0.84	N/A	flexure
	3	44.00	44.05	1.00	N/A	pure shear

Table 4-1 (Contd.)

		V_{exp} [kN]	$V_{t,num}$ [kN]	R_{FE}	Failure mode	
					Experimental	Numerical
Li et al. [43]	B01	43.33	48.73	1.13	shear	pure shear
	B02	58.67	60.03	1.02	shear	pure shear
	B03	56.67	69.03	1.22	shear	pure shear
Sato et al. [44]	S2	160.50	182.40	1.14	diagonal tension	pure shear
	S3	202.10	197.50	0.98	peeling	flexure
	S4	156.30	173.30	1.11	peeling	pure shear
	S5	198.20	197.50	0.99	flexural tension	flexure
Beber [45]	V9	105.77	126.34	1.19	shear	pure shear
	V10,11	105.40	179.77	1.71	shear	pure shear
	V12,18,20	127.92	126.45	0.99	shear	pure shear
	V12,14	96.65	90.99	0.94	shear	pure shear
	V19	116.77	148.36	1.27	shear	pure shear
	V13	123.88	127.37	1.03	shear	pure shear
	V15,16	125.39	189.42	1.51	shear	pure shear
	V16,18	193.20	172.49	0.89	shear	pure shear
	V22,20	127.71	113.62	0.89	shear	pure shear
	V21,22	130.65	115.32	0.88	shear	pure shear

	Mean	St. Dev.	COV	Min	Max
All Beams	1.08	0.21	0.19	0.78	1.71
Pure shear	1.11	0.22	0.19	0.78	1.71
Mixed shear	1.04	0.13	0.13	0.91	1.20
Flexure	0.92	0.08	0.09	0.80	0.99

* Disagreement between experimentally observed and numerically identified failure mode

5. FRAME ANALYSIS

FE analysis of a two-dimensional (2D) RC frame was performed to model a realistic structure and to check if the frame FE developed in this study is able to identify shear failures and the effect of FRP shear retrofit in terms of strength of RC frames. An experimentally tested RC frame [57], with externally bonded FRP shear retrofit, was considered in this study.

The RC frame was a two-story single-bay frame with geometric and mechanical properties representative of a cement plant preheater tower structure [57]. The frame had a height of 4.6m and width of 2.3m, and the depth and width of the beams and columns were 400mm and 300mm, respectively. The compressive strength of concrete was 43MPa. No. 20 bars with yield strength 447MPa were used as longitudinal reinforcement in all beams and columns. No. 10 bars with yield strength 455MPa were used for stirrups in the columns, and US No. 3 bars with yield strength 506MPa were used for stirrups in the beams.

The RC frame was tested in two phases: (a) Phase I: loading of the RC frame without FRP retrofit; and (b) Phase II: loading of the RC frame after FRP retrofit. During both the phases of testing, a constant axial load of 420kN on each column, and a variable horizontal load at the mid height of the second story beam were applied on the frame.

During the Phase I testing, the frame was subjected to a forward lateral drift of 1.0%, which caused significant shear damage in the beams. The maximum horizontal load applied to the frame and the corresponding displacements were measured experimentally during the testing as 327kN and 44.7mm, respectively. The beams showed significant shear damage, and the failure of the frame was assumed to be imminent.

Carbon FRP was used to retrofit in shear the first and second story beams after they sustained significant damage in Phase I of the experimental testing, as shown in Figure 5-1. The carbon

FRP was applied as strips of width 150mm, 1mm thickness and center to center spacing of 337.5mm. The tensile strength, elastic modulus and ultimate strain of the carbon FRP were 876MPa, 72.4GPa and 0.121 respectively. Phase II testing was performed on the retrofitted RC frame by applying horizontal displacement cycles with progressively increasing amplitude. The frame showed a flexural mode of failure and the maximum horizontal load was measured as 421.5kN, with a horizontal displacement equal to 78mm.

5.1 Finite element analysis of frame

A FE model of the 2D RC frame was built using the force-based frame element developed in this research study. The FE mesh for the considered RC frame consisted of six nodes and six elements (see Figure 5-1). The total height and width of the frame was 4.0m and 1.9m respectively, measured along the centerline of the structural members. The dashed line shown in Figure 5-1 represents the full dimensions of the frame. Fixed boundary conditions were applied at nodes 1 and 2.

Five Gauss-Lobatto integrations points were employed in each element and the cross sections were discretized into twenty layers each. The constitutive models adopted to describe the stress-strain behavior of concrete and steel were the Kent-Scott-Park model [50] and the bilinear hysteric model with kinematic hardening, respectively.

The shear strength at any monitored cross section is given by Equations (4.3) and (4.2) (see Section 4.3). The shear strength contribution of the concrete, (V_c), was computed as [58],

$$V_c = 0.9 \cdot d \cdot b \cdot \left(0.075 \cdot {f_c}^{2/3}\right) \cdot \max\left(1, 1.6 - d\right) \cdot \min\left[2,\ 1+40 \cdot \max\left(\frac{A_{sb}}{b \cdot d}, \frac{A_{st}}{b \cdot d}\right)\right] \quad (5.1)$$

$$\left(\text{units: N, mm}\right)$$

The shear strength contribution of steel was computed according to Equation (2.4) (Section 2.4.2). The strength contribution of the FRP was computed according to the newly proposed model (see Chapter 3).

A displacement controlled loading technique was applied based on the Newton-Raphson iterative procedure. A lateral displacement was incrementally applied at node 5 and a constant vertical axial load of 420kN was applied on each column at nodes 5 and 6.

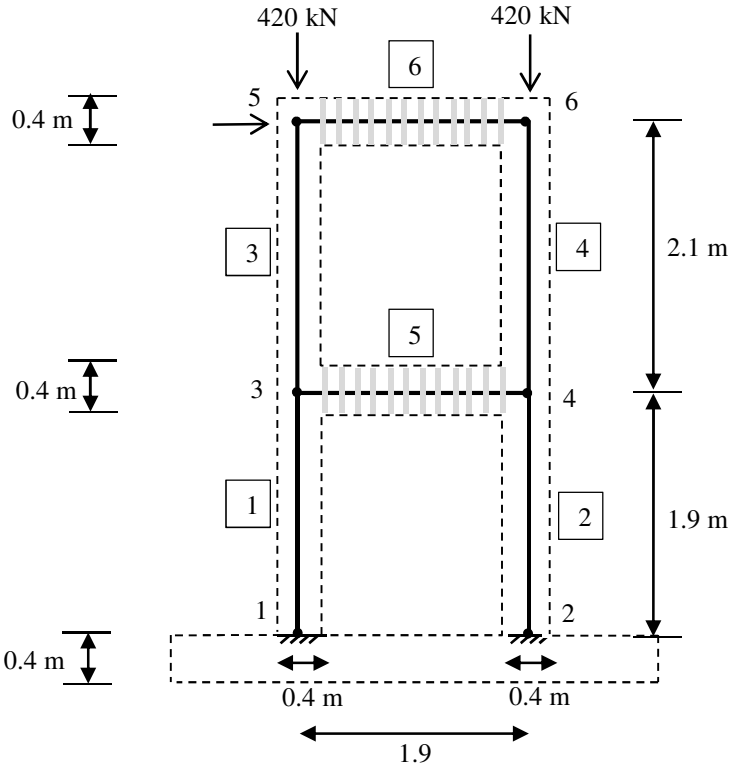

Figure 5-1: FE mesh of the frame

5.2 Comparison of results for the 2-D RC frame

The 2D frame was analyzed using FEDEASLab and the developed FE model. The numerical response was obtained for the both phases of testing. Figure 5-2 shows the comparison of the numerical and experimental results for the lateral force and horizontal displacement at node 5 for Phase I testing. The maximum lateral load obtained from the finite element analysis is 328.7kN

and the computed relative error is 0.52%. Figure 5-3 shows the comparison of the numerical and experimental results for the lateral force and displacement at node 5 for Phase II testing. The maximum lateral load obtained from the FE analysis is 386.2kN and the computed relative error is -8.38%. The FRP shear retrofitted frame has a ductile failure mode and the ultimate load carrying capacity of the frame increased by 57.5kN. It is observed that the comparison between the displacement for the numerical and experimental responses is not satisfactory. This is due to the fact that the FE model neglects the shear deformations in the elements and the rotations at the base of the columns, which are modeled as fixed in the FE analysis.

In addition, due to limitations of the computational platform FEDEASLab, the second phase of loading for the specimen was modeled starting from undamaged conditions and not from the actual damaged conditions reached at the end of the first phase of loading. This discrepancy between the actual frame specimen and the FE model could explain the differences in the stiffness observed in Figure 5-3 between the numerical and experimental response of the frame in Phase II.

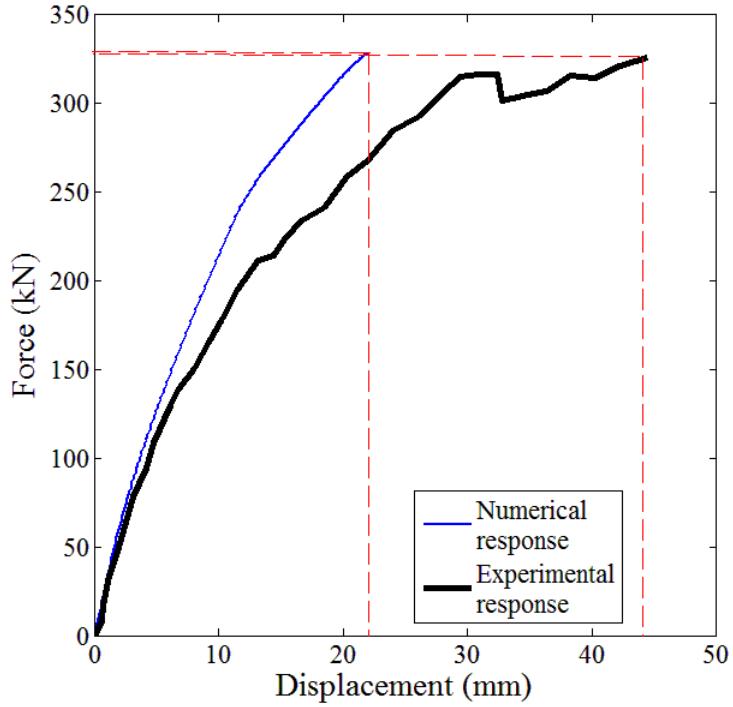

Figure 5-2: Comparison of numerical and experimental results for Phase I testing: lateral force-displacement

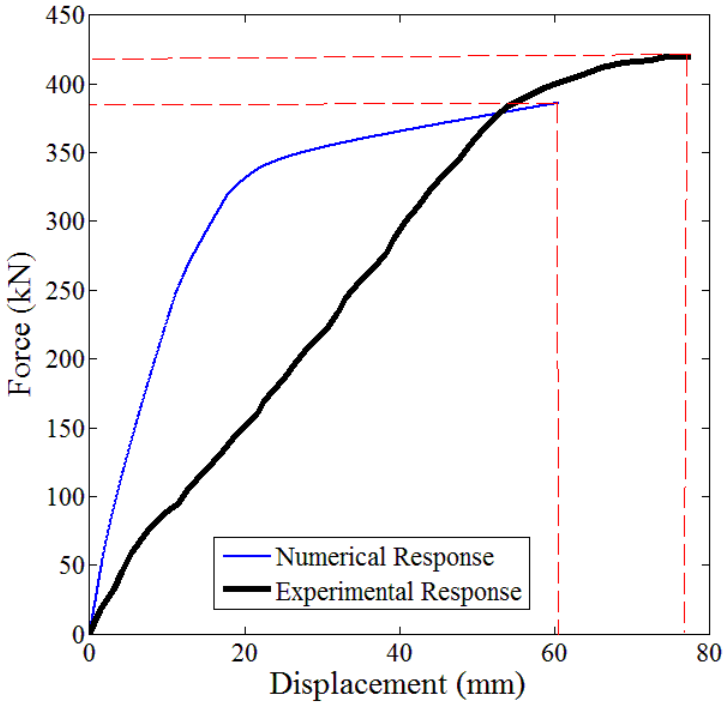

Figure 5-3: Comparison of numerical and experimental results for Phase II testing: lateral force-displacement

6. CONCLUSIONS AND RECOMMENDATIONS FOR FUTURE WORK

The objective of this research was to efficiently model reinforced concrete (RC) beams strengthened in shear with externally bonded fiber reinforced polymers (FRP). A new shear strength model to accurately compute the shear strength increase of RC beams due to retrofit with FRP was proposed in this study. Furthermore, a frame finite element was developed to accurately simulate the nonlinear finite element (FE) response of RC beams and frames retrofitted with FRP.

The newly proposed shear strength model can compute the FRP shear strength contribution to the total strength of a RC beam for the following three types of FRP retrofit techniques: (a) side bonding, (b) U-jacketing, and (c) wrapping. The accuracy of the newly proposed model was evaluated based on experimental results available in the literature and compared with the other models considered in this study in terms of the following two parameters: (a) ε_{theo}, defined as the relative percentage of error of the theoretically computed FRP shear strength contributions with respect to the corresponding experimental results, and (b) R_{theo}, defined as the of ration between the theoretical and experimental FRP shear strength contributions. It was observed that, the newly proposed model is able to predict the FRP shear strength increase with overall better accuracy than the other models considered in this study. The proposed model has an excellent agreement with the experimental results for FRP in side bonding. However, improvements are still needed in estimating the FRP shear strength increase in the cases of retrofit using U-jacketing and wrapping.

The accuracy of the frame FE developed in this study was determined by comparing the load carrying capacity obtained from the numerical simulations with the corresponding experimental results. It was observed that the new FE is able to identify the following failure modes: (a) pure

shear, (b) mixed flexure-shear, and (c) flexure. The agreement between the numerical and experimental response of RC beams is overall very good in terms of shear strength and failure mode.

The newly proposed frame element was used to model a 2D RC frame that was retrofitted with FRP. The numerical response of this frame with and without FRP shear retrofit was computed. Good agreement between the numerical and experimental load carrying capacities was found for both Phase I (without FRP retrofit) and Phase II (with FRP retrofit) testing. The FE model results in terms of deflections and displacements were not in good agreement with the experimental results due to the fact that the proposed frame element does not model shear deformations in the elements and to other limitations of the computational platform adopted in this study. However, the frame FE developed in this study was able to identify shear failures in the RC beams and the 2D RC frame with and without FRP retrofit.

Based on the research presented in this study, the following recommendations for future research are proposed:

a) To verify the accuracy of the proposed model for various FRP shear retrofit configurations individually, more RC beams retrofitted in U-jacketing and wrapping are required to be experimentally tested and numerically analyzed.
b) The proposed model can compute the FRP shear strength contribution for RC beams with $a / d \geq 2.5$. More research is required to model the failure behavior of FRP shear retrofitted RC beams with $a / d < 2.5$.
c) The frame FE proposed in this study is limited to RC beams with rectangular cross section. Additional research is needed to model the nonlinear response of T-section RC beams retrofitted with FRP in shear.

REFERENCES

[1] Teng T.G., Cheng J.F., Smith S.T., Lam L. *FRP: strengthened RC structures*. John Wiley and Sons 2002.

[2] Commission of the European Communities. Eurocode No.2: Design of Concrete Structures, Part 1: General Rules and Rules for Buildings. *ENV* 1992-1-1 2003.

[3] ACI Committee 440. Guideline for the design and construction of externally bonded FRP systems for strengthening of concrete structures (ACI 440.2R-02). *American Concrete Institute* 2002.

[4] MacGregor J.G., Wight J.W. *Reinforced concrete: Mechanics and Design*. Prentice Hall 2008.

[5] Bazant P.Z., Kim J.K. Size effect in shear failure of longitudinally reinforced beams. *ACI Journal* 1984; 81:456-468.

[6] Bazant P.Z., Yu Q. Designing against size effect on shear strength of reinforced concrete beams without stirrups. *Journal of Structural Engineering* 2005; 131(12):1877-1885.

[7] Arslan G. Cracking shear strength of RC slender beams without stirrups. *Journal of Civil Engineering and Management* 2008; 14(3):177-182.

[8] Arslan G. Shear strength of reinforced concrete beams with stirrups. Materials and Structure 2008; 41:113-122.

[9] Bukhari I.A., Ahmad S. Evaluation of shear strength of high-strength concrete beams without stirrups. *Arabian Journal for Science and Engineering* 2007; 33(2B):321-336

[10] Song J., Kang W.H. Probabilistic shear strength models for reinforced concrete beams without shear reinforcement. *Structural Engineering and Mechanics* 2010; 31(1):15-38.

[11] Kuo W.W., Cheng T.J., Hwang S.J. Force transfer mechanism and shear strength of reinforced concrete beams. *Engineering Structures* 2012; 32:1537-1546.

[12] Zararis P.D. Shear strength and minimum shear reinforcement of reinforced concrete slender beams. *ACI Structural Journal* 2003; 100(2):203-214.

[13] Tureyen A.K., Frosch R.J. Concrete strength: another perspective. *ACI Structural Journal 2003*; 100(5):609-610.

[14] ACI Committee 318. Building code requirements for structural concrete (ACI 318-08) and Commentary. *American Concrete Institute* 2008.

[15] Khalifa A., Gold W.J., Nanni A., Aziz A.M.I. Contribution of externally bonded FRP to shear capacity of RC flexural members. *Journal of Composites for Construction* 1998; 2(4):195-198.

[16] Khalifa A., Nanni A. Improving shear capacity of RC T-section beams using CFRP composites. *Cement and Concrete Composites* 2000; 22:165-174.

[17] Triantafillou T.C., Antonopoulos P.C. Design of concrete flexural members strengthened in shear with FRP. *Journal of Composites for Construction* 2000; 4(4):198-205.

[18] Triantafillou T.C. Shear strengthening of reinforced concrete beams using epoxy bonded FRP composites. *ACI structural Journal* 1998; 95(2):107-115.

[19] Chen J.F., Teng J.G. Anchorage strength models for FRP and steel plates bonded to concrete. *Journal of Structural Engineering* 2001; 127(7):781-794.

[20] Chen J.F., Teng J.G. Shear capacity of FRP-strengthened RC beams: FRP debonding. *Construction and Building Materials* 2003; 17: 27–41.

[21] Monti G., Liotta M. Tests and design equations for FRP strengthening in shear. *Construction and Building Materials* 2007; 21(4):799-809.

[22] Monti G., Renzelli M., Luciani P. FRP adhesion to uncracked and cracked concrete zones. *Proceedings of the 6th International Symposium of Fiber Reinforce Polymer (FRP) Reinforcement for Concrete Structures (FRPRCS-6)* Singapore 2003.

[23] Taljsten B. Strengthening concrete beams for shear with CFRP sheets. *Construction and Building Materials* 2003; 17: 15-26.

[24] Al-Sulaimani G.J., Sharif A., Basunbul I.A., Baluch M.H., Ghaleb B.N. Shear repair for reinforced concrete by fiberglass plate bonding. *ACI Structural Journal* 1994; 91(3):458-464.

[25] Chaalla O., Nollet M.J., Perraton D. Shear strengthening of RC beams by externally bonded side CFRP strips. *Journal of Composites for Construction* 1998; 2(2):111- 113.

[26] Malek A.M., Sadaatmanesh H. Ultimate shear capacity of reinforced concrete beams strengthened with web bonded fiber reinforced plastic. *ACI Structural Journal* 1998; 95(4):391-399.

[27] Pellegrino C., Modena C. Fiber reinforced polymer shear strengthening of reinforced concrete beams with transverse steel reinforcement. *Journal of Composites for Construction* 2002; 6(2):104-111.

[28] Mutsuyoshi H. Behavior of concrete beams strengthened in shear with carbon fiber sheets. *Journal of Composites for Construction* 2004; 8(3):258-264.

[29] Perera R, Barchín M, Arteaga A, Diego A.D. Prediction of the ultimate strength of reinforced concrete beams FRP-strengthened in shear using neural networks. *Composites: Part B* 2010; 41:287-298.

[30] Diagana C., Li A., Gedalia B., Delmas Y. Shear strengthening effectiveness with CFF strips. *Engineering Structures* 2003; 25:507-516.

[31] Bousselham A., Chaallal O. Shear strengthening reinforced concrete beams with fiber-reinforced polymer: assessment of influencing parameters and required research. *ACI Structural Journal* 2004; 101 (2):219-227.

[32] Maeda T., Yasuyuki A, Sato Y., Ueda T., Yoshio K. Study on bond mechanism of carbon fiber sheet. *Proceedings of the Third International Symposium on Non-Metallic (FRP), Japan Concrete Institute* Japan 1997; 1:279-286.

[33] Aprile A., Benedetti A. Coupled flexural-shear design of R/C beams strengthened with FRP. *Composites:Part B* 2003; 35:1-25.

[34] Zhang Z., Cheng T.T.H. Shear strengthening of reinforced concrete beams using carbon fiber reinforced polymer laminates. *Journal of Composites for Construction* 2005; 9(2):158-169.

[35] Cao S.Y., Chen J.F., Teng J.G., Hao Z. Debonding in RC beams shear strengthened with complete FRP wraps. *Journal of Composites for Construction* 2005; 9(5):417-428.

[36] Miyauchi K., Inoue S., Nishibayashi S., Tanaka Y. Shear behavior of reinforced concrete beam strengthened with CFRP sheet. *Transactions of the Japan Concrete Institute* 1997; 19:97-104.

[37] Uji K. Improving shear capacity of existing reinforced concrete members by applying carbon fiber sheets. *Transactions of the Japan Concrete Institute* 1992; 14: 253-266.

[38] Taerwa L., Khalil H., Matthys S. Behaviour of RC beams strengthened in shear by external CFRP sheets. *Proceedings of the Third International Symposium Non Metallic (FRP) Reinforcement for Concrete Structures, Japan Concrete Institute* Japan 1997; 483–90.

[39] Umezu K., Fujita M., Nakai H., Tamaki K. Shear behavior of RC beams with aramid fiber sheet. *Proceedings of the III International Symposium Non Metallic (FRP) Reinforcement for Concrete Structures, Japan Concrete Institute* Japan 1997; 491–98.

[40] Adhikary B.B., Mutsuyoshi H. Behavior of concrete beams strengthened with carbon-fiber sheets. *Journal of Composites for Construction* 2004; 8: 258-264.

[41] Funakawa I., Shimono K., Watanabe T., Asada S., Ushijima S. Experimental study on shear strengthening with continuous fiber reinforcement sheet and methyl methacrylate resin. *Proceedings of the III International Symposium Non Metallic (FRP) Reinforcement for Concrete Structures, Japan Concrete Institute* Japan; 1997; 475–82.

[42] Park S.Y., Naaman A.E., Lopez M.M., Till R.D. Shear strengthening effect of R/C beams using glued CFRP sheets. *Proceedings of the International Conference on FRP Composites in Civil Engineering*, Hong Kong, China 2001; 1: 669–676.

[43] Li A., Diagana C., Delmas Y. Shear strengthening effect by bonded composite fabrics on RC beams. *Composites: Part B* 2002; 33: 225-239.

[44] Sato Y., Ueda T., Kakuta Y., Tanaka T. Shear reinforcing effect of carbon fiber sheet attached to the side of reinforced concrete beams. *Advanced composite materials in bridges and structures, 2nd International Conference,* Canada 1996; 11-14.

[45] Beber A.J. Comportamento Estrutural de Vigas de Concreto Armado Reforcadas com Compositos de Fibra de Carbono. Ph.D. Thesis, Universidade Federal do Rio Grande do Sul, Porto Alegre, Brasil 2003.

[46] Spacone E., Filippou F.C., Taucer F.F. Fiber beam column model for non-linear analysis of R/C frames: Part I. Formulation. *Earthquake Engineering and Structural Dynamics* 1996; 25:711-725.

[47] Spacone E., Filippou F.C., Taucer F.F. Fiber beam column model for non-linear analysis of R/C frames: Part II. Applications. *Earthquake Engineering and Structural Dynamics* 1996; 25:727-742.

[48] Neuenhofer A., Filippou F.C. Evaluation of non-linear frame finite element models. *Journal of Structural Engineering* 1997; 123(7):958-966.

[49] Conte J.P., Barbato M., Spacone E. Finite element response sensitivity analysis using force based frame models. *International Journal for Numerical Methods in Engineering* 2004; 59:1781-1820.

[50] Kent D.C., Park R. Flexural members with confined concrete. *Journal of Structural Division ASCE* 1971; 97(7):1969-1990.

[51] Priestley M.J.N, Verma R., Xiao Y. Seismic shear strength of reinforced concrete columns. *Journal of Structural Engineering, ASCE* 1994; 120:2310-2329.

[52] Filippou F.C., Constantinides M. FEDEASLab getting started guide and simulation examples. *Technical Report NEESgrid* 2004.

[53] Matlab, High performance numeric computation and visualization software, Users Guide. *The MathWorks Inc., Natick, MA* 1997.

[54] Seismic design guidelines for highway bridges. *ATC- Applied Tech. Council* 1981.

[55] Barbato M. Efficient finite element modeling of reinforced concrete beams retrofitted with fibre reinforced polymers. *Computers and Structures* 2009; 87:167-176.

[56] Cladera A., Mari A.R., Shear design procedure for reinforced normal and high strength concrete beams using artificial neural networks. Part II: beams with stirrups. *Engineering structures* 2004; 26:927-936.

[57] Kim S.W., Vecchio F.J. Modeling of shear-critical reinforced concrete structures repaired with fiber-reinforced polymer composites. *Journal of Structural Engineering ASCE* 2008; 134(8):1288-1299.

[58] Eurocode 2. Design of concrete structures. *The European standard EN* 1992-1-1:2004.

VITA

Srinivasa Anusha was born in 1987 in Visakhapatnam, India. She graduated with her bachelor's degree from College of Engineering, JNTU Kakinada, India, in Civil Engineering in May 2009. She started her Master's degree in Structural Engineering at Louisiana State University in fall 2009. She holds a graduate assistantship at Communications and Disorders Laboratory, LSU since spring 2012. She has been working on her research since spring 2010 and expects to receive the degree of Master of Science in Civil Engineering in May 2013.